UNIVERSITY OF CALIFORNIA, MERCED

Positron Emission Tomography (PET)/Computed Tomography (CT) Guided Diffuse Optical Tomography (DOT) for Breast Cancer Imaging

A thesis submitted in partial satisfaction of the requirements for the degree

Master of Science

in

Biological Engineering and Small – scale Technologies

by

Kavita Kumar

Committee in charge:

Professor Changqing Li, Chair

Professor Joel Spencer

Professor Kara McCloskey

2018

The Thesis of Kavita Kumar is approved, and is acceptable in quality and form for publication on microfilm and electronically:

(Professor Changqing Li)

(Professor Joel Spencer)

(Professor Kara McCloskey)

University of California, Merced

2018

TABLE OF CONTENTS

LIST OF FIGURES

LIST OF TABLES

ACKNOWLEDGEMENTS

I would like to thank those who have made this research possible. I would like to first express my utmost gratitude to my adviser, Dr. Changqing Li, for his continuous support and his time investment in helping me succeed. I would like to thank my committee members, Dr. Kara McCloskey and Dr. Joel Spencer. Through her strong work ethic and wonderful personality Dr. McCloskey has always been a role model for me. I would like to thank Dr. Joel Spencer for joining my committee at last notice and for our wonderful conversations which helped me prepare for the defense. I would like to thank my lab members for welcoming me and for creating a positive work environment. I would specifically like to thank Dr. Yue Zhao for being more of a big sister than a lab mate. I would like to thank the School of Engineering and Graduate Division for working with me in finishing the degree. I would like to thank all the friends I made during my graduate studies, for it was because of them I looked forward to going to school every day. I would like to thank my dearest Angela Yu for her honesty and love. I would like to thank my family for their continuous patience, understanding and support throughout my journey. Most importantly, I would like to thank Eli, for it was the conversations we had regarding the research and the confidence he has in me that brought me this far today.

ABSTRACT OF THESIS

Positron Emission Tomography (PET)/Computed Tomography (CT) Guided Diffuse Optical Tomography (DOT) Study for Breast Cancer Imaging

by

Kavita Kumar

Master of Science in Biological Engineering and Small – scale Technologies

University of California, Merced, 2018

Professor Changqing Li, Chair

Diffuse optical tomography (DOT) is known to be a promising imaging technique for breast cancer detection. It involves the detection of transmitted light photons in the near infrared range through soft biological tissues. It can provide functional images of oxyhemoglobin, deoxyhemoglobin, water and lipid content in breast tissue. DOT itself is low – cost and uses non – ionizing light. However, it is ill – posed and has low spatial resolution. Structural prior information from other imaging modalities can be used to counter these issues. Computed tomography (CT) utilizes high - energy x-ray photons to obtain high spatial resolution images and can provide good structural information for DOT. Positron emission tomography (PET) is a nuclear medicine imaging technique that can be used to observe the metabolic processes in the body. A PET/CT guided DOT imaging system can be used for therapeutic monitoring during neoadjuvant chemotherapy in breast cancer patients.

In this study, Clinical PET and CT breast images containing a breast tumor is used to create 3D meshes using the finite element mesh method. The process involves applying an edge detection algorithm to the CT images. The breast tumor location is extracted from the PET images via a thresholding method. After the breast mesh is made, the breast tumor location is interpolated to the breast mesh nodes. Two different breast meshes are compared in this study. Three different detector based setups for the two breast mesh cases are compared. The soft prior method of reconstruction is used which

requires the use of structural prior information from the CT images and segmentation. The results presented are for the two different breast mesh cases and compare different noise levels. The reconstruction results validate the feasibility of the design and optimization of the optical detectors and laser sources for a future physical PET/CT guided DOT imaging system.

Chapter 1

Overview

1.1 Breast Cancer Research Overview

1.1.1 History

Breast cancer is the deadliest cancer among women in the United States [1]. Contrary to popular belief, 85% of breast cancers occur in women who have no family history of it [1]. The remaining percentage of breast cancer occurs from gene mutations inherited by one's mother or father. As of today, 1 in 8 American women will develop invasive breast cancer during her lifetime [1].

Before the 2000's breast cancer death rates were increasing every year [1]. In the 1970's surgeons would perform radical mastectomy as soon as a breast lump was biopsied [2]. During that time breast cancer was an unspeakable disease and breast preservation treatments were not considered. In 1972, the Breast Cancer Detection and Demonstration Project (BCDDP) was founded and promoted self-breast cancer screening [2]. For the next 20 years there was much rallying to the federal government by popular celebrities, wives of important politicians, journalists and many advocacy groups. This allowed for $210 million from the Department of Defense (DOD) to be allocated for breast cancer research in the fiscal year of 1993 [2]. Since then, over $2 billion has been appropriated to the Breast Cancer Research Program (BCRP) [2]. In 1995, it was reported that San Francisco Bay Area had the highest incident rates of invasive breast cancer in the world [3]. This report led to the formation of the California Breast Cancer Research Program (CBCRP) which studied the environmental factors, lifestyle habits and risk factors related to breast cancer [2] . The results from the study conducted by CBCRP showed a need for a transdisciplinary research program and after much lobbying to congress, Breast Cancer and Environment Research Centers (BCERCs) were formed. With 7 years of funding, the purpose of the BCERCs was to bring together biologists, epidemiologists, clinicians, stakeholders, advocates and many scientists to pioneer a novel model for conducting research. Due to the investment in transdisciplinary research methods, breast cancer incidence rates have been decreasing in the United States at a rapid rate. However, it is still expected that 40,920 women will die due to breast cancer in the year 2018 [1]. There is still a large need for awareness and advances in detection methods.

1.1.2 Diagnosis

The first step of treatment is adequately diagnosing breast cancer. The diagnosis process involves analyzing the abnormal findings at the clinician's office from the palpation exam. About 80% of breast cancer cases are diagnosed from finding breast masses during the palpation exam [4]. These masses are single, hard and have a less smooth surface. Bloody nipple discharge, skin changes, abnormalities of the nipple and areola, and swollen lymph nodes can also provide implications of breast cancer [4]. It's important to understand that many breast lumps may show up during the palpation exam, but they may be benign and not cancerous. These non-cancerous breast lumps may just be abnormal growth and should be monitored for changes [5].

Most breast cancers are ductal cancers which means they begin in the ducts that carry milk to the nipple. Another common type are lobular cancers which involve cancer in the glands that make breast milk. Once the cancer becomes malignant it can spread to other parts of the body through the lymph system. The lymph system are collections of immune system cells that can allow for breast cancer cells to drain into under the arm, around the collar bone and inside the chest. Knowing that breast cancer cells can spread and create cancer in other areas of the body such as the chest makes it a deadly disease [5].

1.1.3 Current commonly used imaging methods for detection

This sub-section provides an overview of the current commonly used imaging methods for detection which include: mammography, breast ultrasound, magnetic resonance imaging (MRI) and positron emission tomography (PET). Note: histopathological examination is also a common detection method but is invasive [4].

Mammography

The United States Preventative Services Task Force (USPSTF) recommends all women to start routine breast cancer screening using mammograms after the age of 50 [6]. Mammograms involve placing the patient's breast on a flat support plate then compressing with a parallel plate. X-rays then pass through the breast and are captured by detectors [7]. Compression makes dense breasts more difficult to image since they can "mask" the cancerous regions. As age of the patient increases the amount of fat in breasts also increase and these fatty regions appear dark on mammograms. The compression of breasts with fatty regions may cover up the small cancers during imaging which can make early detection difficult [7]. Mammography has multiple advantages and disadvantages. Some advantages are that it is the only appropriate method of mass screening for American women [8]. Every year mortality due to breast cancer is reduced because of yearly mammogram screening. It also prevents use of aggressive therapies and the need for more expensive screenings. However, mammograms do involve ionizing

radiation risk to women which can cause cancer. It also results in false positive reports which prompt for unwanted biopsies [8].

Digital Breast Tomosynthesis is a common 3D mammography technique where x-rays are taken at different angles to create cross-sections. It uses a slightly larger dose of x-ray radiation than standard mammography [7].

The American College of Radiology (Breast Imaging-Reporting and Data System, or BI-RADS) has four groups that separate mammographic densities which include: fat, fibroglandular tissue, heterogenic density and extremely dense [7]. This differentiation is important for distinguishing different breast cancer risks and is the only classification of mammographic density used clinically [7].

Breast Ultrasound

Ultrasound uses high – frequency sound waves and is feasible for women with suspected breast lesions. Its advantages are that it can be used for young, pregnant or lactating women that have breast lesions. It can also be used to analyze lesions after artificial breast implantation. Lastly, it can be used as an alternative confirmation for palpable masses and lesions [4]. Some disadvantages are that it may not be good for early detection because of poor spatial resolution [4].

Magnetic Resonance Imaging (MRI)

MRI uses magnetic fields to produce cross-sectional images and is very good for the soft tissues of the breast. The use of molecular gadolinium – based contrast agent, which is injected intravenously, can provide high sensitivity for detecting breast cancer. However, MRI is a very expensive imaging modality[9] . It is associated with giving close to 20% false positives reports and 1% false negative results due to technological limitations. Only women who have a high risk of breast cancer such as family history, genetic testing and a review of clinical history are the best candidates for MRI exams [9].

Positron Emission Tomography (PET)

PET uses FDG (fludeoxyglucose) as a contrast agent for tumor detection [10]. FDG is a radioactive analog of glucose and can be used to mark the increased metabolic activities of the rapidly growing breast cancer cells. It is highly sensitive and demonstrates high sensitivity for malignant lesions. However, studies have shown that PET is not suitable for early detection which requires the ability to detect small (< 1.0 cm) breast masses [10]. It has also been seen demonstrate a high number of false – negative reports. This makes PET imaging not suitable for small and low – grade lesions [11].

1.2 DOT Overview

1.2.1 DOT background

Diffuse Optical Tomography (DOT) is a very lucrative imaging modality because it is non-ionizing, non-invasive and a low-cost technique [12]. The breast tissues contributing mainly to their optical properties, such as the absorption coefficient and the reduced scattering coefficient, are mainly composed of hemoglobin and water which have a low absorption window in the 650-950 nm [12]. This allows for near infrared (NIR) light to be transmitted over the breast tissues. The absorption coefficient is referred to as μ_a and the reduced scattering coefficient is referred to as μ_s [13]. The point at which the light is emitted is referred to as the source position. The optical photons from the source are propagated inside breast tissues. Most of them are scattered and absorbed. A few of them are diffused to the breast surface to be detected with typical optical detectors such as charge-coupled devices (CCD), photomultiplier tube (PMT), or photodiodes. The source and detectors are placed with different designs[14].

The photon propagation inside breast tissue can be modeled by the diffusion equation, which can be solved by a finite element method (FEM) based on a finite element mesh [12]. This is referred to as the forward modeling. The reconstruction of DOT imaging can be performed by minimizing the differences between the forward model predictions and the physical measurements. An inverse problem is solved by updating the chromophore concentration at each node in the mesh [14].

The low – cost, non – invasive and non – ionizing benefits of DOT makes it a very lucrative imaging modality. However, DOT has low spatial resolution and is an ill-conditioned inverse problem. Photon scattering also makes it difficult to pinpoint breast tumor position and size. The purpose of the rest of chapter 1 is provide detail on each of the subjects covered in subsection 1.2.1.

1.2.2 Advantages of performing DOT

There are many advantages to performing DOT. It is safe to use because of its non – ionizing radiation and it is low cost. Near infrared light used in DOT can penetrate through 10 cm of tissue which allows for imaging of the entire breast [12]. The tissue bulk optical properties obtained provide chromophore concentration maps of the water, lipid and oxy – and deoxy – hemoglobin. This information can allow for measuring changes in the optical properties of the breast during neoadjuvant chemotherapy [13].

A recent study published by Columbia University used DOT to measure the 2 – week percent change in DOT hemoglobin concentrations associated with breast cancer [15]. They analyzed the residual cancer burden (RCB) in breast cancer patients by performing DOT before neoadjuvant chemotherapy (NACT) and after [15]. NACT has been performed for decades and is also known as primary chemotherapy [16]. NACT is given to patients because of its ability to decrease the size and extent of the tumor as a

breast-conserving treatment [16]. The purpose of using DOT while monitoring NACT is to help patients determine the need for breast removal surgery or mastectomy. In the study by Columbia University, DOT imaging was performed before the initiation of NACT and every two weeks up to the time before surgery took place. In their outcomes, they were able to see the association between the 2-week percent change of deoxyhemoglobin, hemoglobin and water fraction as well as the assessment of the RCB response [15]. They specified that there are numerous other imaging modalities that can also evaluate the biological activity of breast tumors such as MRI and PET. However, those imaging modalities require injection of intravenous contrast agents, are time consuming and even expose the patient to radioactive ionizing components that can cause cancer [15]. This study by Columbia University was a motivating factor of my feasibility study because they proved the positive implications of using DOT in safe and efficient breast cancer neoadjuvant chemotherapy monitoring.

1.2.3 DOT systems

Continuous Wave

This subsection provides a brief overview of the general DOT systems. The primary interest in this study is the continuous wave (CW) based method because of its low cost, simplicity and high signal – to – noise ratio [17]. Light beams from laser modules are transmitted to an optical switch. This switch passes the beams individually to preselected points on the breast surface via source fiber bundles. There can be a ring structure that holds the source and detector fiber bundles. The light photons collected by the detector units are converted into voltage signals. These signals are then collected by the computer through a data acquisition board [17]. Alternatively, a charge coupled device (CCD) camera can be used instead of the detector fiber bundles to develop the 3D imaging of the entire breast. This single detection element and imaging window can reduce the number of calibration coefficients that come from using multiple detector elements [18].

Frequency Domain

Another DOT instrument design is the frequency – domain system. It uses intensity modulated light to allow for measurement of the intensity and phase which is influenced by absorption and diffusion coefficients. The system requires time to scan multiple frequencies. A past study has shown the use of a single source – single detector scheme to allow for fast multiplexing and minimization of data acquisition time [19]. This single – source – single detector schematic includes linear translation stages that allow for source and detector multiplexing. A 100 ms sample of source and detector signals are taken at 10 kHz for a total of 256 measurements. The system in the study had errors such as the drift of the detectors and that not all measurements have the same AC or DC intensities. The source – detector arrangement variations in transmitted intensity between fibers also ranged up to 30%. However, despite the errors in the study the combination of

intensity modulated signal detection and iterative image reconstruction can be feasible for tumor detection [19].

Time Domain

In the time domain system, measurements are made at multiple times and require time to average enough signal for achieving acceptable results. It consists of injecting picosecond pulses and can localize deep perturbations (depth > 3 cm) [20]. It can increase depth sensitivity with increased photon traveling time allowing for collection of different measurements with different spatial sensitivity. It requires the use of high – quantum efficiency time – domain detectors and has low measurement speed. Due to the cost of sources, detectors and timing electronics, it is not widely used [20].

1.2.4 DOT modeling and reconstruction

This subsection provides an overview of the forward model and reconstruction method of DOT.

The radiative transfer equation (RTE) also known as the Boltzmann transport equation is used to model photon propagation in biological tissue medium. In time domain the RTE is given as [21]

$$\left(\frac{1}{c}\frac{\delta L}{\delta t} + \hat{s}.\nabla L(r,t,\hat{s}) + (\mu_s + \mu_a)L(r,t,\hat{s}) = \right. \tag{1.1}$$

$$\mu_s \int_{4\pi} L(r,t,\hat{s}')f(\hat{s},\hat{s}')d^2\hat{s}' + q(r,t,\hat{s})$$

With L being the energy transfer per unit time and radiance being L(r,t, $\hat{s}$), and $q(r,t,\hat{s})$ is the source of the inside, and f($\hat{s},\hat{s}'$) is the scattering phase function. The spatial location and angular direction of the discretization are implemented, and the equations are derived in RTE. The first order simplification of the RTE is the diffusion equation shown below [21]

$$\left(-\nabla.k(r)\nabla + \left(\mu_a(r) + \frac{j\omega}{c}\right)\right)\phi(r,\omega) = q_o(r,\omega) \tag{1.2}$$

This equation is in the frequency domain, where the frequency is $\omega = 2\pi f$ and k(r) is the diffusion coefficient, ϕ(r) is the photon flux density at position r, c is the speed of light and μ_a(r) is the absorption coefficient. The zero – frequency case of the frequency domain is the continuous wave.

In the continuous wave domain, the propagation of near infrared light in breast tissue is modeled by solving the diffusion equation [22], seen below as

$$-\nabla \cdot [k(r)\, \nabla\, \Phi\, (r)] + \ \mu_a(r)\Phi(r) = \ \mathcal{Q}_o(r) \tag{1.3}$$

$\Phi(r)$ is the photon density, $\mathcal{Q}_o(r)$ is the isotropic light source at position r, ∇ is the gradient operator, $\mu_a(r)$ is the absorption coefficient and $k(r)$ is the optical diffusion coefficient which is defined below as [22]

$$k(r) = \frac{1}{3[\ \mu_a(r) + \ \ \mu_s'(r)]} \tag{1.4}$$

with $\mu_s'(r)$ being the reduced scattering coefficient. The air – tissue boundary is represented by the refractive index mismatch. The following equation accounts for the internal reflection of light back into the tissue [23]

$$-2\alpha\hat{n} \cdot k(r)\nabla\phi(r) = \ \Phi(r) \tag{1.5}$$

where $\hat{n}$ is the unit normal vector to boundary surface and α depends on the refractive index mismatch between the air and tissue [22]. α is determined by the difference between the measurement data and the numerical calculations obtained from the forward model. Photons are modeled propagating through the breast tissue using the finite element mesh method. In this method, the volume of the breast is divided into small elements and the diffusion equation is solved at the nodes that connect these elements. This allows the photon density, Φ, to be obtained [12].

By solving the DOT inverse problem, the optical absorption maps can be obtained. However, DOT is known to be ill – posed so regularization methods are used in the reconstruction. The first step is iterative minimization of the quadratic error between the modeled and measured data [24]:

$$\Omega = min_{\mu_a}\{\left|\left|y - F(\mu_a)\right|\right|_2^2 + \ \lambda|| \ L(\mu_a - \ \mu_{a0})||_2^2\} \tag{1.6}$$

where Ω is the objective function to minimize, λ is the regularization parameter, L is the dimensionless penalty matrix which is obtained from another structural imaging modality[22]. If information from another structural imaging modality is not available then L can be replaced with an identity matrix I [22] . The Jacobian, or sensitivity matrix, is found for each iteration. This sensitivity is the $\Delta\phi/\Delta\mu_a$ at each node in each measurement. Since continuous wave measurements are simulated in this study, only the absorption coefficients are recovered [12]. The scattering coefficients are considered constant and known. There is update after each iteration of difference calculation between the measured and modeled data. This updating equation or the Levenberg –

Marquardt algorithm is based on the nonlinear Newton iterative method seen below as [25] [26] [27]:

$$(J^T J + \lambda L^T L)\delta\mu_a = J^T(y - F(\mu_a)) \quad (1.7)$$

Here, J is the Jacobian (sensitivity matrix) with a dimension of M x N. M is the number of measurements and N is the number of nodes. The L matrix is calculated before the reconstruction from another imaging modality. The update is seen by $\delta\mu_a = \mu_a - \mu_{a0}$. The maximum number of iterations used in this study is 20. When convergence occurs, the solution is accepted [22].

1.2.5 DOT for breast cancer

The use of non-ionizing near infrared light makes DOT a safe imaging modality. This has enabled it to be performed on women in a large age group ranging from about 38 – 60 years of age[28]. It can also be performed on pre-menopausal women down to about 30 years of age to menopausal elderly women as well [29] . The decision for whether a woman is suitable for DOT is determined by the clinician, largely depending on the stage of the cancer.

DOT is useful for identifying different tissue types in the breast. The tissues found in the breast include adipose, fibroglandular and tumorous tissues [12]. Fibroglandular tissue has higher water and hemoglobin content where adipose tissue has higher lipid content. The recovered chromophore concentrations during DOT imaging such as hemoglobin, water and lipid content can allow for distinguishing between the different breast tissue types thereby allowing for calculation of percent breast density. Breast density is an independent risk factor for breast cancer that is based on the amount of fibroglandular tissue present within the whole breast volume [12].

DOT can be used to measure different types of tumors depending on size as well. The smallest lesion DOT itself can accurately quantitively image are cysts ranging down to the size of 15 mm [28]. Cysts are different from solid breast tumors in sense that they have lower absorption and scattering coefficients compared to the surrounding normal tissue [30]. Solid tumors have higher absorption and scattering coefficients compared to the normal surrounding tissues [30]. DOT can also distinguish different types of tumors including benign tumors such as fibroadenoma and malignant tumors such as invasive ductal carcinoma [31]. The ability to accurately quantitively image different tumor types depends on the size of the tumor and inflammation in the imaging area [31].

1.3 Multimodal Imaging Overview

1.3.1 Structural guidance

Structural or anatomical imaging modalities include Computed Tomography (CT), Magnetic Resonance Tomography (MRI) and ultrasound. These imaging modalities provide high resolution morphological information. CT can allow for precise assessment of the size and location of tumors. CT uses x – ray radiation and too much x – ray exposure can lead to development of cancer. Ultrasound can have difficulty in defining the location of the tumors. However, ultrasound is a non – ionizing and portable imaging modality. MRI can allow for better differentiation between regions where the tumor is location. However, it is very high cost and requires the use of contrast agents [32].

1.3.2 Functional imaging modalities

Popular functional imaging modalities include optical tomography and Positron Emission Tomography (PET).

Optical tomography uses non – ionizing near – infrared photons in the wavelength range of 650 to 950 nm. The photons can reach a depth of up to several centimeters which allows soft tissues like the breast and brain to be important regions of interest. It can allow information relating to the oxy- and deoxyhemoglobin content to be collected which are physiological markers of cancer to due fast cancer cell growth. Its non – invasiveness and ability to provide functional information makes it a lucrative imaging method. However, optical tomography has low spatial resolution [33].

Positron Emission Tomography can be used as noninvasive metabolic monitoring [34]. Patients with microscopic and macroscopic breast cancer can be differentiated after the first round of chemotherapy using FDG PET. Early information of tumor can be helpful in determining the best therapeutic strategy for patients. First, a radioactive substance such as FDG (2-[18F]-fluoro-2-deoxy-D-glucose) is injected into the patient [35]. Then, after about 60 – 120 minutes the patient is brought in for the scan. The positron emitted from the FDG collides with the electron in the tissue of the patient. This annihilation reaction produces two 511 keV gamma rays that are captured by the detectors [35]. PET scan can be used in conjunction with chemotherapy to see the tumor glucose metabolism. When the glucose metabolism of the tumor decreases, it can be concluded that the tumor is decreasing itself. In past research this has proven to be a substantial promise in noninvasive metabolic marking in cancer treatment [34]. Despite the benefits of PET, it also has low spatial resolution and provides low structural imaging capability.

There is no imaging modality that can provide both high functional sensitivity and high resolution for anatomical structures. Therefore, the combination of two or more imaging modalities is desirable [36].

1. 4 Anatomical Guidance Overview

1.4.1 Anatomical guidance applications in different imaging modalities

CT guided PET

CT guided PET combines anatomic and metabolic imaging information to improve monitoring in response to therapy. FDG – PET can be limited in its ability to detect small primary breast tumors [11]. However, integrated PET/CT can provide accurate localization of functional data with high – resolution anatomical CT images. In a previous study, patients have been able to use the dedicated PET/CT system [37]. Here, an initial CT scan is done followed by a PET scan. Then the reconstructed x – ray attenuation – corrected PET images are fused with corresponding CT images. This study has resulted in low false – negative findings and diagnosis of recurrent tumor in breast cancer patients at 90% success rate [37].

MRI guided PET

MRI guided PET contributes to clinical management of breast cancer. It is feasible and produces high quality images. In a previous study, 36 patients received a single contrast injection of 18F - FDG and underwent dual – imaging protocol for the PET/MRI scan [38]. The results showed identification of 74 positive lesions which supports feasibility of the machine in a clinical setting. Despite the benefits, PET/MRI has a longer delay time between tracer administration, longer bed positioning and longer data acquisition time [38].

CT guided FMT

FMT is fluorescence molecular tomography and uses fluorescence signals for low – cost and ionizing – radiation free imaging. The use of fluorescent biomarkers can be used to monitor tumor growth and evaluate therapy methods [39]. However, FMT is ill – posed and photon scattering is primarily in the low energy visible light photon propagation of tissue. CT can be used as a structural prior for FMT. CT guided FMT can allow for construction of robust diffusion models. It can also provide high quality reconstruction and increase specificity for tumor detection [39] .

1.4.2 Anatomical guidance for DOT

DOT spatial resolution can be improved by anatomical guidance through other imaging modalities. Different types of anatomical image guided DOT imaging include, MRI – DOT, Ultrasound guided DOT, and combination of optical and x – ray tomosynthesis for breast imaging [40]. Several studies have shown that multimodal

imaging such as MRI and DOT together can allow for high – resolution structural information and functional parameters of cancers to be obtained [41] . This study uses CT/PET guided imaging as a structural prior for DOT imaging.

Structural Priors for DOT

There are two known methods of incorporating anatomical guidance into DOT image reconstruction: hard prior method and soft prior method [40]. Hard prior must have uniform optical properties in the same region. Hard prior method has a strong bias in incomplete or incorrect structural priors. Soft prior method can allow for smooth changes in the reconstructed optical properties of different regions. But there must be region segmentation done by an expert. Kernel method can allow for incorporation of priors without target region segmentation [40]. Neighboring voxels can be used to capture structural information from anatomical images. The kernel algorithm has been applied in previous research to reconstruct dynamic PET images of breast cancer and has achieved good results [42]. In this study the soft prior method is compared along with different noise levels. The soft prior method for reconstruction is further explained in detail in Chapter 3.

PET/CT anatomical guidance for DOT

While DOT is known to be low – cost, non – ionizing and efficient it also has low spatial resolution. This can lead to false positive results which can give patients stress and lead to unnecessary tests and biopsies. The use of dual model imaging of PET can be combined to overcome false positive report [42]. Furthermore, the kernel method can improve spatial resolution and the accuracy of the reconstructed DOT images. It can model the PET image intensity as a function of feature points obtained from prior information. A previous study with computed tomography guided DOT multimodal imaging reported that the soft prior method provides a negligible amount of false positive data [40]. However, the kernel method provides no false positive report [40]. This information was proven by analyzing real clinical CT breast images from a woman with a 2cm tumor mass. The study of CT guided DOT with the kernel method gives good background for the study of PET guided DOT [40].

1.5 Thesis Outline

This thesis describes a PET/CT guided DOT method and system build for breast cancer imaging. It presents numerous models and simulations which validate the feasibility of the results. In the system set up, the CT will be used to obtain the breast structural information. Then, the PET will be simultaneously used to obtain the tumor information from the breast. The simultaneous use of the PET/CT will help correct for attenuation in the PET imaging. Afterwards, DOT will be performed in a timely manner alongside neoadjuvant chemotherapy to monitor tumor changes. DOT is chosen because of its use of non-ionizing near infrared light which is safe and low cost. This study

provides insight on ability for a PET/CT guided DOT system to be used for safe and efficient therapeutic monitoring.

Chapter 2 describes the finite element mesh method used to create breast mesh models. The meshes are used to solve the diffusion equation, which is important for DOT imaging. The breast meshes are specifically generated from breast CT images using edge detection via MATLAB. The mesh is also used to find the real tumor location based on prior information from the PET images. The results show a 3D model of the breast and its respective tumor location. Two different meshes are compared to see if a different mesh type has a distinct effect on the DOT simulations. One of the DOT simulations performed after obtaining the mesh is the forward modeling. The results from the forward modeling show how the DOT photons propagate through the breast. This chapter also compares the forward modeling results from the different breast meshes used. This chapter concludes by comparing the different detector setups and also provides experimental schematic drawings for the ring detector based and camera based imaging systems.

Chapter 3 describes the reconstruction that is performed in this study. The reconstruction simulations result in information about the optical properties of the breast tissue. The reconstruction performed is the soft prior method which requires the use of structural prior information which in this study are from the CT/PET images. The results presented are for the two different breast mesh cases and compare different noise levels. Three different detector based setups are also compared for the two distinct breast mesh cases with and without noise.

This purpose of Chapter 3 is to use the reconstruction results to validate the feasibility of the design and optimization of the optical detectors and laser sources for a future physical PET/CT guided DOT imaging system.

Chapter 4 presents the conclusion for this thesis and implications for future studies.

Chapter 2

FEM Mesh Generation for DOT Imaging

2.1 Introduction

The purpose of the first part of this chapter is to provide an overview of the finite element mesh (FEM) generation method and its importance. The advantages of the mesh are explained in relation to the equations for the forward modeling and reconstruction covered in section 1.2.4. Some background is provided on the current popular FEM software. Lastly, the mesh generation approach used for this study is briefly described.

The second section of this chapter first describes the method by why which the mesh was generated from clinical breast CT images for this study. Then the method by which the breast tumor information was acquired from the PET images is described. The breast tumor generated plot is interpolated to match the breast mesh. Two different breast mesh cases are compared. Three different detector setups are presented for the two breast mesh cases. Experimental schematic drawings are presented for the ring detector based and camera based imaging systems. Finally, the forward modeling results from the two different breast mesh cases are presented. These results are used for the reconstruction done in Chapter 3.

2.2 Overview of FEM Mesh Generation

2.2.1 FEM background

The finite element method (FEM) is used to solve differential equations numerically on a finite element mesh. The mesh is composed of many mesh elements which divide a geometrical domain into smaller regions known as a mesh element. Each mesh element has several finite element nodes. For the tetrahedral mesh, each element has four nodes. The differential equation is solved by finding solutions in a finite number of nodes in the mesh. The unknown parameters are approximated using known base functions and are based on the nodes. The equations in the finite element method are integrated over each element and summed over the entire geometric domain [43].

Mesh Generation Technique

The finite element method is a very powerful tool but creating the mesh can be very error – prone if done manually. Recognizing this concern, numerous methods have been devised to automate the mesh generation. Some methods include: mesh topology first, nodes first, adapted mesh template and nodes and elements simultaneously [44]. The basis of the mesh are mainly triangles and quadrilaterals because they have defined angles which make them good discretized elements. Triangles and quadrilaterals in 2D

can also be easily converted into triangles and quadrilaterals of similar sizes. Common mesh generators make a mesh of triangles by creating all the nodes then connecting them. The Delaunay triangulation maximizes the sum of the smallest angles of the triangles and is obtained by connecting points associated with neighboring polygons [44]. Some mesh generation methods are not able to generate an initial mesh that is good enough. They require postprocessing techniques to improve the mesh. Steps of postprocessing techniques include first subdividing elements of the desired type, then refining elements to compatible sizes and finally applying a mesh smoothing technique. The overall quality of the mesh can be compared by element type, element shape, mesh density control and time efficiency [44].

FEM for DOT Modeling

The finite element method is used in this study to model the optical photon propagating through breast tissues. The whole volume of the breast is divided into discrete elements and the photon propagation is modeled by solving the diffusion equation [12]. (The diffusion equation, forward modeling and reconstruction equations are explained in detail in section 1.2.4.) In the forward modeling, the source and detector positions are assigned. The breast tissues are assigned appropriate optical properties such as the absorption coefficient and the reduced scattering coefficient which can be obtained from literature [45]. From the forward model, the measurements can be predicted and calculated. The inverse problem is specifically solved for obtaining the reconstructed optical absorption maps by minimizing the difference between the measurements and the predicted values [12]. The next subsection describes some popular FEM mesh generation software. The mesh generation software used in this study is also explained.

2.2.2 Popular FEM mesh generation software

Below are a few common FEM mesh generation software. Note that not all mesh generation software are listed and explained in detail here.

NIRFAST

NIRFAST was originally developed in 2001 by Dartmouth University. It can import medical images from conventional imaging systems like MRI and CT. It can then segment the images and create NIRFAST – compatible finite element meshes. Then those meshes can be used to model near – infrared light propagation and allow for creation of reconstructed images of chromophore maps. This software tool is helpful for modeling an optical system with multi – modal imaging capabilities. It is a sophisticated MATLAB – based package [23][46].

Toast++

Toast++ is an open – source software environment developed by the University College London. It has a hierarchical set of core libraries written in C++ for matrix

computation, finite – element computation and iterative parameter reconstruction. The finite – element subsystem has the Mesh class which represents essentially the mesh components including node coordinates and list of elements. Toast++ has support for different element types as well. It most importantly can solve the forward and inverse problems in DOT. It has a set of libraries that can simulate the near – infrared light propagation in a heterogenous media. It also uses a range of regularization parameters which allow for the possibility of incorporating structure priors. Despite being written in C++, it can include MATLAB and PYTHON bindings to allow for a rich toolset [47].

TetGen

TetGen is the software used in this study for generating 3D tetrahedral meshes. It was developed by Weierstrass Institute for Applied Analysis and Stochastics (WIAS) in Germany. For a 3D polyhedral domain, TetGen generates the constrained Delaunay tetrahedralization. Delaunay – based algorithms can preserve arbitrary complex topology and geometry. The input domain of TetGen is given as a piecewise linear complex (PLC) which means the boundary of each cell in set is a union of cells and that if two distinct cells intersect then their intersection is a union of cells [48]. This PLC must be given by users as an input. This can make the mesh generation difficult because the quality of the input given by users must be robust. The input should not have self – intersections and must be watertight. TetGen provides many commands to work around complex inputs since there is no clear definition for the term "mesh quality [48]."

The next section will provide steps on how the mesh was generated from clinical breast CT images for this study using TetGen. Then describe the process by which the tumor location was taken from the PET images and then interpolated from the breast mesh. Finally, the chapter will end by comparing different mesh cases with their respective forward modeling results.

2.3 Mesh Generation Results

2.3.1 Edge Detection with CT images

As described in the TetGen subsection, it is necessary to develop a robust 3D input with well-defined and evenly spaced points to make the mesh [48]. The foundation of the mesh in this study were clinical breast CT images obtained from a patient from UC Davis Medical Center. 512 separate images were received and together formed the 3D geometry of her breast. These images were viewed using Amide which is a free software tool for multimodal medical image analysis [49]. Below, Figure 2.1 show sample single images from the 512 total that were received. Amide can allow the user to scroll through the images to view the patient's entire breast.

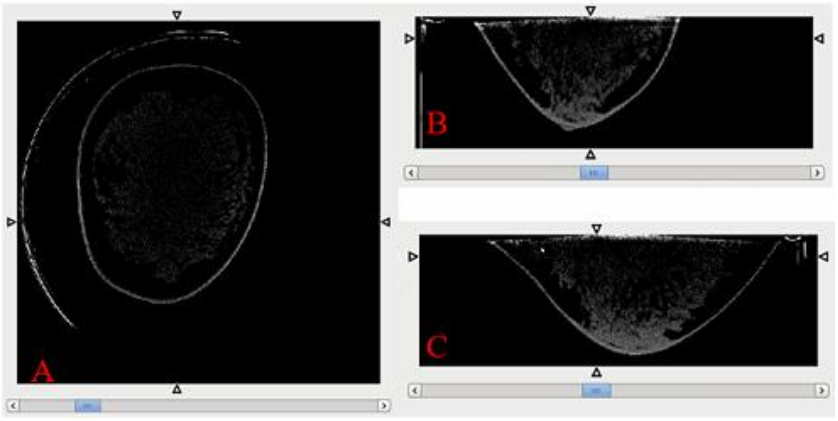

Figure 2.1: Different views of patient's breast CT scans used in this study [49]. (A) transverse view. (B) coronal. (C) sagittal. All 512 images of patient's breast can be viewed by scrolling through.

After receiving the images and viewing them using Amide, they were converted into DICOM file type [49]. This allowed for the images to opened with MATLAB. The goal was to develop a 3D matrix with well - defined and evenly distributed points using the CT breast images. These points could then be imported into TetGen to create the mesh. As seen in Figure 2.1 the breast contains a bright edge which defines the shape. 'Sobel' was found to be an efficient edge detection method in MATLAB which could detect the bright spots in the images. A high threshold value was used to only capture the outside breast points and not the internal points. The 'Sobel' edge detection method was looped over every image in MATLAB to create the 3D breast geometry. However, the 'Sobel' method was not efficient for creating evenly distributed points. As mentioned in the TetGen subsection, intersecting points would not be a sufficient input for mesh creation [48]. To overcome this constraint, the point cloud obtained after the edge detection was redefined using polyshape then a boundary was found to evenly space the points. A MATLAB provided function interpac was then used to space 40 points per slice (or image). A point grid was then defined at the top and bottom of the breast. It is important to note that the artificially placed control on left side of the breast seen in Figure 2.1(A) was manually removed.

The 3D breast geometry was then shifted to the origin to allow for the tumor obtained from the PET images to be plotted together. The points were shifted because there were only 300 PET images. The pixel sizes and spacing (thickness) between the PET and CT images were different as well. Below are the equations applied to the 3D breast geometry point matrix.

$$X = (X' - 256) * 0.41 \tag{2.1}$$

$$Y = (Y' - 256) * 0.41 \tag{2.2}$$

$$Z = (Z' - 256) * 0.135 \tag{2.3}$$

With X', Y' and Z' representing the initial inputted values and X, Y and Z representing the final values. Figure 2.2 shows the final breast 3D geometry created.

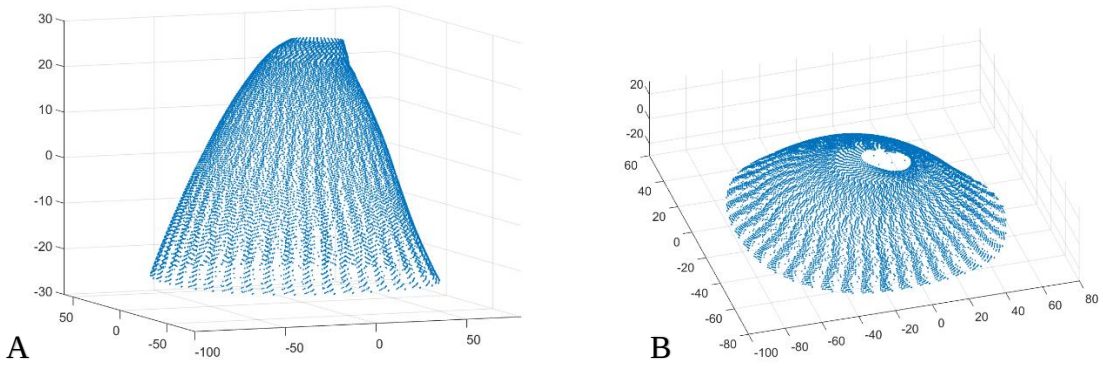

Figure 2.2: 3D breast geometry point cloud. (A) Front view. (B) Top down view.

Both (A) and (B) are the same breast, created from the clinical breast CT images. (B) is a rotated version of (A). The 80th image slice to the 470th image slice. There is a point grid added to the top and bottom portions of the breast. There are no internal points. These changes were made to make the 3D breast geometry points suitable for the mesh generation.

After the points were shifted the breast mesh was generated using TetGen. Figure 2.3 shows the generated breast mesh.

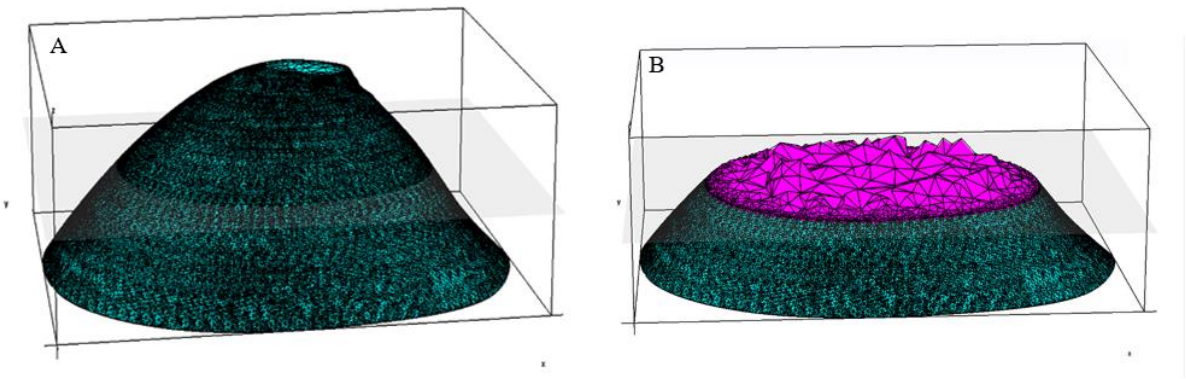

Figure 2.3: Generated breast mesh from 3D breast geometry points. (A) shows the full breast. (B) is a cut plane of the breast geometry to show the size of the internal tetrahedral.

2.3.2 Interpolation of tumor geometry from PET

This subsection describes the procedure by which the tumor location was obtained from the PET images. Then, the process by which the tumor obtained points were

interpolated to match the breast mesh points is described. It was necessary for tumor obtained points from the PET images to match the breast mesh points from the CT images for the forward modeling and reconstruction to be done because the tumor has no contrast in the CT images.

The same patient who underwent CT scans also performed PET scans at the same position. The CT images and the PET images have the same coordinate. 300 PET images of her breast were obtained for this study. These images were viewed using Amide [49] . Below, Figure 2.4 show sample single images from the 300 total that were received.

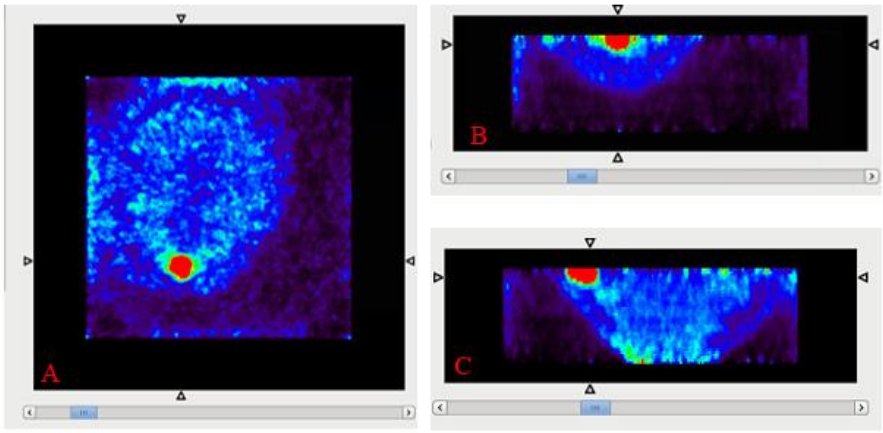

Figure 2.4: Different views of patient's breast PET scans used in this study [49]. (A) transverse view. (B) coronal. (C) sagittal. All 300 images of patient's breast can be viewed by scrolling through. The bright red spot represents the patient's tumor size and location.

After receiving the PET images and viewing them using Amide, they were converted into DICOM file type [49]. This allowed for the images to be opened with MATLAB. The goal was to develop a 3D matrix of points describing the breast tumor location and size. Since the tumor is very bright compared to the rest of the breast a very high threshold value was set. Then the values matching this threshold or greater were stored. These values were found for every image or slice. After the 3D matrix of points for the tumor was obtained, these points were shifted. The shift allowed for the 3D breast geometry points obtained from the CT to be plotted with points obtained from the PET images. Below are the equations applied to the 3D tumor point matrix.

$$X = (X' - 150) * 0.5 \tag{2.4}$$

$$Y = (Y' - 150) * 0.5 \tag{2.5}$$

$$Z = (Z' - 18.5) * 1.34 \tag{2.6}$$

With X', Y' and Z' representing the initial inputted values and X, Y and Z representing the final values. Figure 2.5 shows the plot of the breast and tumor together after the shift equations were applied.

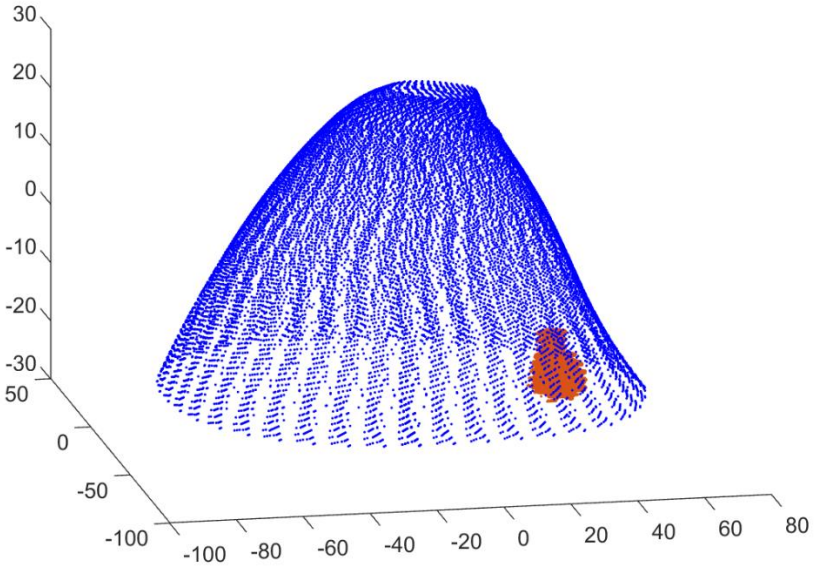

Figure 2.5: Plot of breast and tumor together. The blue points represent the points of the whole breast obtained from the CT images and the orange points represent the points of the tumor from obtained from the PET images.

2.3.3 Mesh cases

This subsection describes 2 different mesh cases. Note that the breast portions used in this study was cut to allow for the reconstruction to be performed in a timely manner. With the entire breast used there would be too many points and reconstruction of the optical maps would not be completed by server or would take many days. The entire tumor was used in both cases.

TetGen generates nodes, elements and faces file. The nodes file contains x,y,z points along with their respective node numbers. The points from these files were used for the rest of simulation and modeling for this study.

Case 1

In the first mesh case, slices 80 – 160 were used and skipped every 2nd slice. Figure 2.6 (A) shows the plot of the portion of the breast mesh used along with the respective tumor points. The tumor points correspond to the breast mesh points. The tumor points were found by using a "dsearchn" function in MATLAB. This function found the closest respective tumor points based on the 3D matrix of points generated from the PET images. Figure 2.6 (B) shows the respective mesh of the portion of the

breast used in case 1. Note that the breast mesh does not contain the tumor location points. Both the tumor points and breast mesh points are stored in two different files.

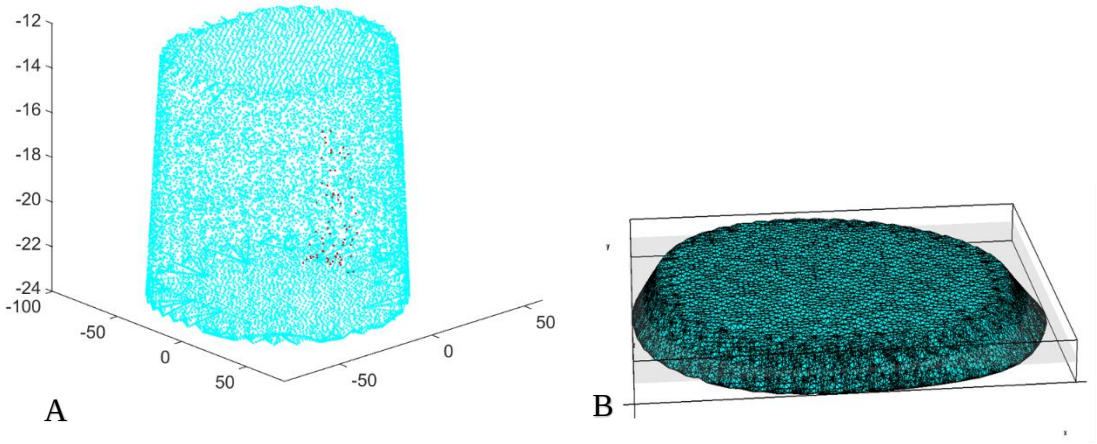

Figure 2.6: Breast nodes plot and respective tumor location for case 1. This case contains 17, 941 nodes, 27,028 faces and 67, 134 elements. (A) is a plot of the breast nodes obtained from TetGen. The blue points are the nodes and 69 orange points are the respective tumor locations. (B) is the breast mesh for case 1. No tumor points are present in the mesh.

Note that there was a reduction in the amount of mesh points corresponding to the tumor location compared to the amount seen in Figure 2.5. This is because there are less internal mesh points. With an increase in the internal mesh points then more corresponding mesh tumor points can be found.

Case 2

In the second mesh case, slices 60 – 220 were used and skipped every 4^{th} slice. This case contains a slightly larger breast portion in terms of height used. Figure 2.7 (A) shows the plot of the portion of the breast mesh used along with the respective tumor points. Again, the tumor points correspond to the breast mesh points and were found by using a “dsearchn” function in MATLAB. Figure 2.7 (B) shows the respective mesh of the portion of the breast used in case 2.

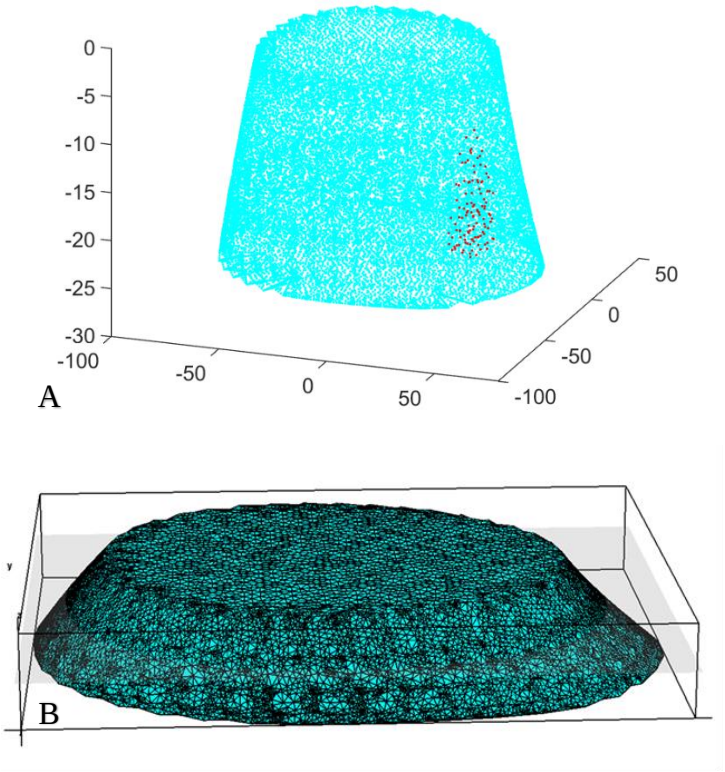

Figure 2.7: Breast nodes plot and respective tumor location for case 2. This case contains 26,367 nodes, 34,430 faces and 107,834 elements. (A) is a plot of the breast nodes obtained from TetGen. The blue points are the nodes and 116 orange points are the respective interpolated tumor points. (B) is the breast mesh for case 2. No tumor points are present in the mesh.

2.4 Forward Modeling Results

2.4.1 Source positions

Real pencil beam source points are used to represent the source positions for this study. For a scattering medium, the real anisotropic source can be approximated by another isotropic source inside the scattering medium. In this study, the source points were first found on the surface of the breast [50] . Then the closest points 1 mm beneath the breast surface were identified. Figure 2.8 below shows the source points found ~1mm beneath the surface for case 1. 42 source points are found for case 1.

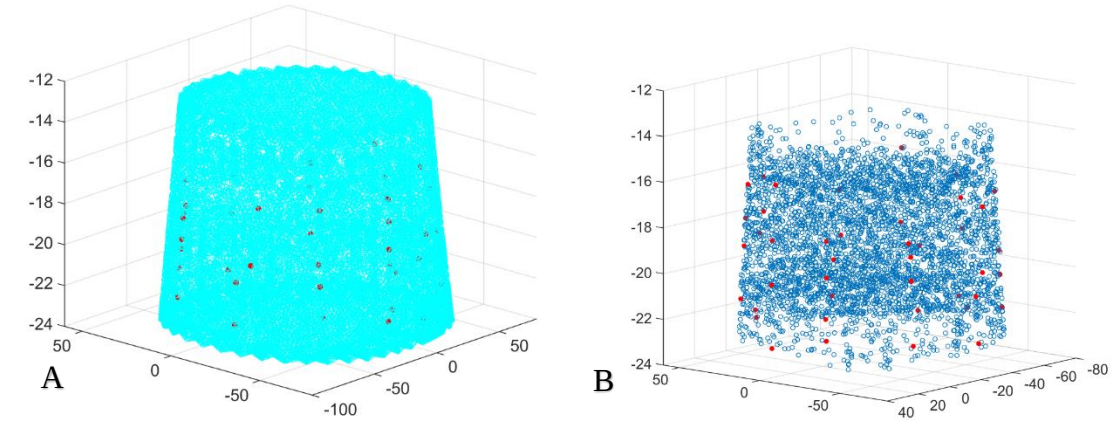

Figure 2.8: Source points for case 1. (A) shows source points found on the surface of the breast. The light blue points represent the breast mesh. The red points represent the source points. (B) shows source points found ~ 1 mm beneath the breast surface. The blue points are the internal breast points. The red points represent the source points on the surface of the internal breast points.

Figure 2.9 below shows the source points found ~1mm beneath the surface for case 2. 44 source points are found for case 2.

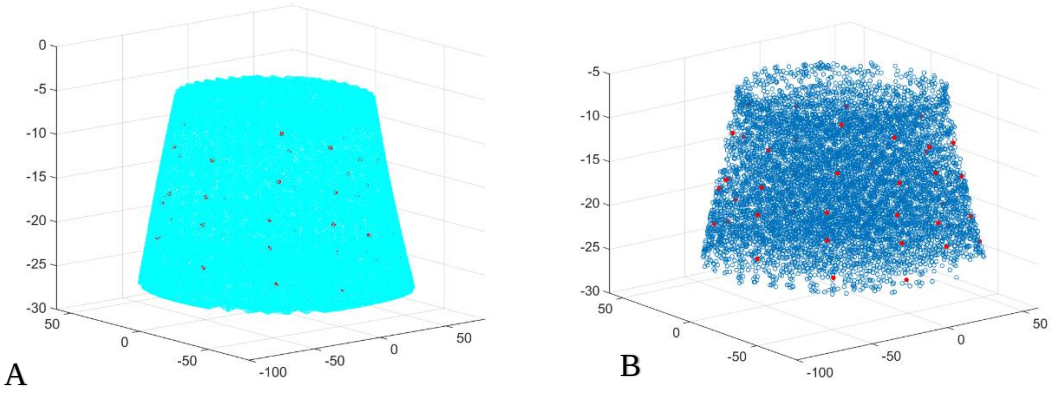

Figure 2.9: Source points for case 2. (A) shows source points found on the surface of the breast. The light blue points represent the breast mesh. The red points represent the source points. (B) shows source points found ~ 1 mm beneath the breast surface. The blue points are the internal breast points. The red points represent the source points on the surface of the internal breast points.

2.4.2 Detector positions

There are three different detector positions compared in this study. These positions include: random detector positioning, ring-based detector positioning and camera based detector positioning. The purpose of different detector positioning is to compare time efficiency and cost with quality of results.

The random detector set up simulates a case with detectors covering the whole surface. The ring-based detector set up simulates a single layer of source – detector pairs setup on a translational stage[17]. For both the random detector setup and the ring – based detector setup, PMTs or photodiodes can be used as photon detectors. PMTs and photodiodes with optical fibers have been used for DOT studies for many years. Through the absorption of light photons, the PMT's emit electrons which are then amplified [51]. Depending on the amount of PMTs or photodiodes that are used and whether an optical fiber switch is implemented this type of set up can result in slow imaging acquisition. For these two types of detectors, measurement noise and thermal noise can be present [51]. The multifiber based set up like the PMT and photodiodes have high flexibility in hardware configuration. The third detector set up compared in this study is using the EMCCD camera. The camera can cover a large surface area of the breast. It is non-contact and can result in plentiful measurement data. It has low – complexity and better portability [52]. However, it has poor sensitivity and high noise compared to the fiber-based detector setups. It can be cost effective as well. However, the ring-based detector set up can also be cost effective because of the fixed number of detectors used and changes in positioning. This can lower the cost and amount of hardware necessary but increase the time spent during image acquisition. The optimal detector set up is analyzed based on the reconstruction results presented Chapter 3.

Random Detector Positioning

The first detector position examined is random detector positioning along the breast surface and covering the whole breast surface. Figure 2.10 shows this positioning for mesh case 1 and mesh case 2.

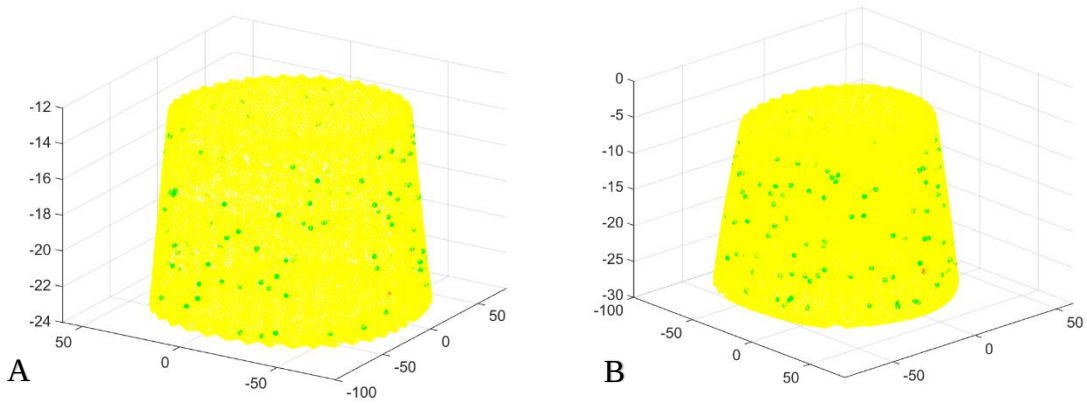

Figure 2.10: Random detector positioning along breast surface. (A) 112 random detector points (green) are positioned along the breast surface (yellow) for each source point (red) for case 1. (B) 188 random detector points (green) are positioned along the breast surface (yellow) for each source point (red).

Ring Based Detector Positioning

The second detector position examined is a ring based detector positioning along the breast surface. A ring of 10 detectors is place along the breast surface then rotated or moved up and down depending upon the source point position. Figure 2.11 shows this positioning for case 1 and case 2. A schematic of this ring structure is seen in chapter 3.

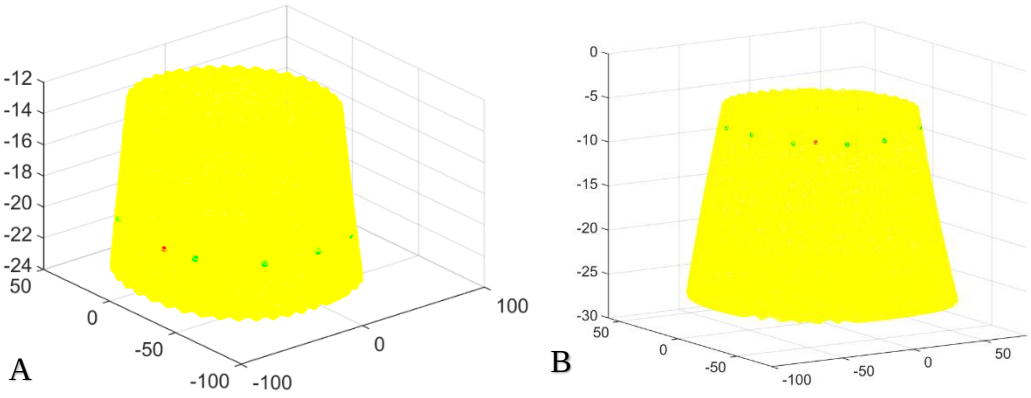

Figure 2.11: Ring based detector positioning. Ring of 10 detectors is placed on breast surface then rotated or moved up and down based on source position. (A) Shows one ring of 10 detector positions (green) for the 15th source point (red) for case 1. There is a total of 420 detector positions. (B) Shows one ring of 10 detector positions (green) for the 44th source point (red) for case 2. There is a total of 440 total detector points.

Since the breast is not a defined geometric shape some layers may only have 9 detector positions. Therefore, both case 1 and case 2 have different amount of detector positions.

Camera Based Detector Positioning

The third detector position examined is the camera based detector positioning along the breast surface. In this setup an EMCCD camera is used to capture a certain portion of the breast surface per source position. Figure 2.12 shows this positioning for case 1 and case 2. Different patches of the breast surface are detected per source point. Mesh case 1 has angle between each patch of 13.92° and Mesh case 2 has angle between each patch of 24°. Both cases have a total of 9 different patches. A few different patches are seen in Figure 2.12.

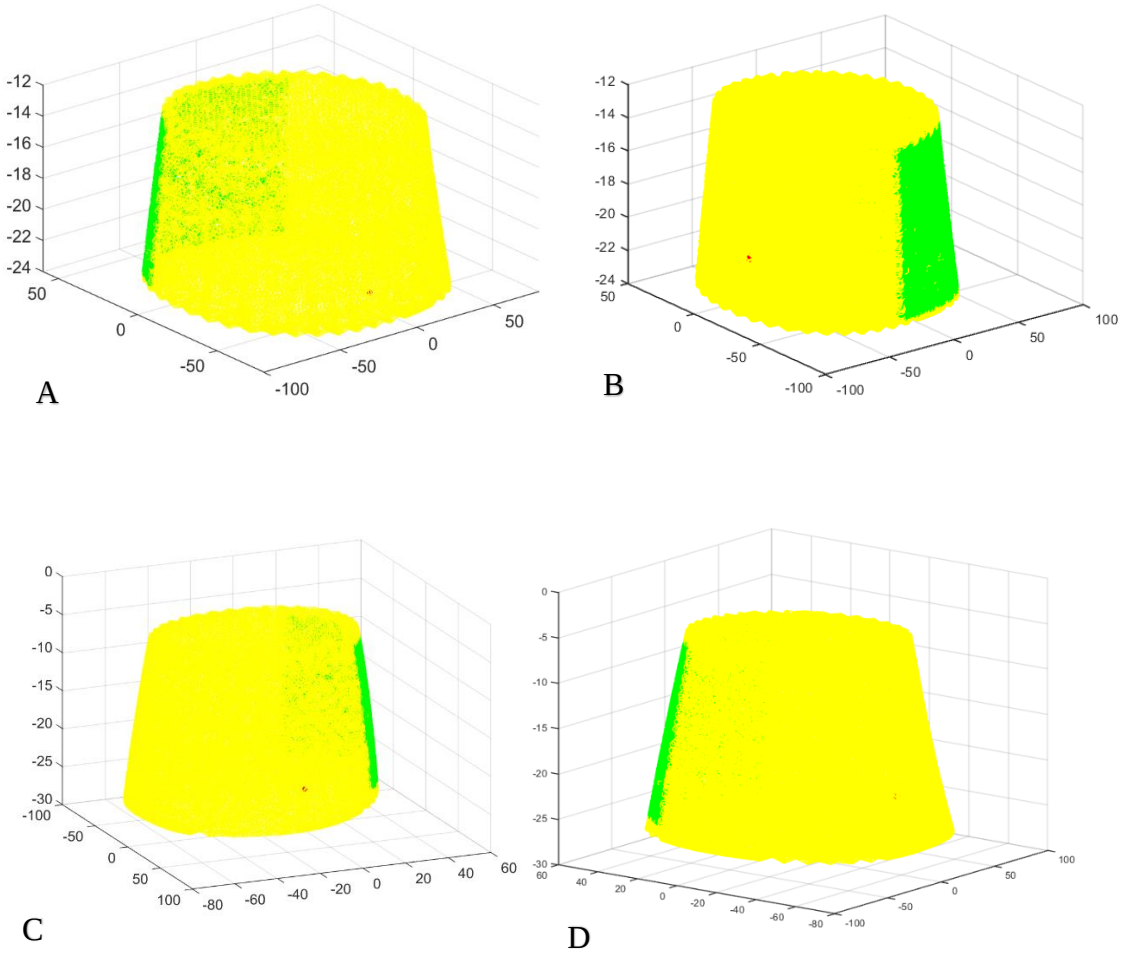

Figure 2.12: Camera based detector positioning. (A) There are 1489 detector positions (green) per source point (red) for case 1. (B) Mesh case 1 with different source point. (C) There are 1912 detector positions (green) per source point (red) for case 2. (D) Mesh case 2 with different source point.

2.4.3 Mask

The mask is the ground truth of the target. The background is set to be 0. Every target node is set to be 1. Figure 2.13 below specifically shows the comparisons of the mask for the case 1 and case 2.

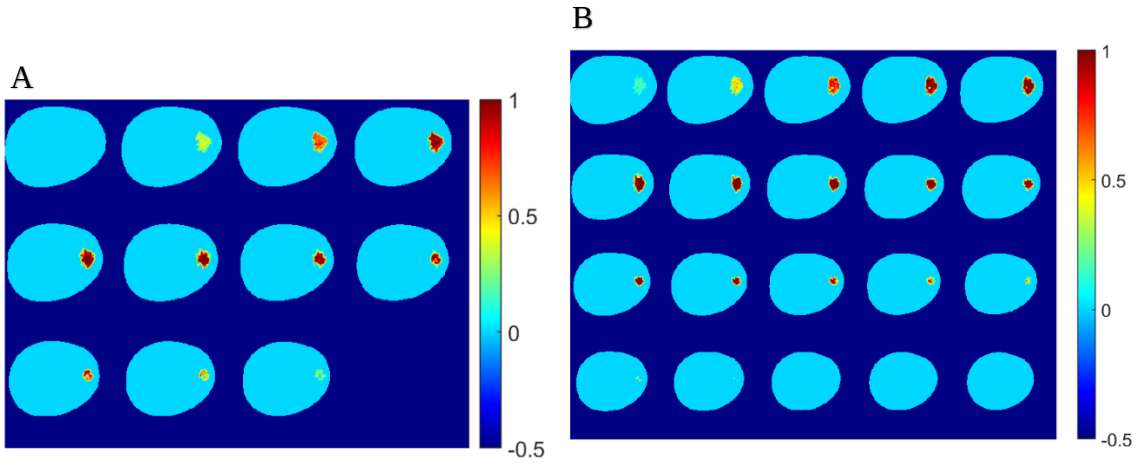

Figure 2.13: Mask for two mesh cases. The dark blue portion is the background. The light blue slices represent the breast slices from bottom to top. The red/yellow regions represent the breast tumor. (A) Case 1. There are less breast slices because a smaller breast mesh is used. (B) There are more breast slices because a larger breast mesh is used.

2.4.4 The absorption coefficient and the reduced scattering coefficient

The initial value of the absorption of the breast was set to be 0.007 mm^{-1} and the initial value of the reduced scattering coefficient of the breast was 1 mm^{-1} [53]. The absorption value for the tumor region of the breast is four times the initial absorption value, 0.028 mm^{-1}. The reduced scattering coefficient was set equal to the initial value. These values were assigned based on literature values from previous studies [53]. The values are outlined in Table 2.1 below. The value of interest in this study was the absorption coefficient to simulate hemoglobin monitoring [53].

Table 2.1: Optical properties for breast and breast tumor for both case 1 and case 2.

	μ_a	μ_s
Background	0.007 mm^{-1}	1 mm^{-1}
Target	0.028 mm^{-1}	1 mm^{-1}

Figure 2.14 and Figure 2.15 show the plots of the absorption and scattering with the defined optical properties. The initial value of the absorption was set to 0.007 mm^{-1} which is why the breast background is greenish color. In Figure 2.15, both the initial and target value of the scattering is set to 1 mm^{-1} which is why both regions are red.

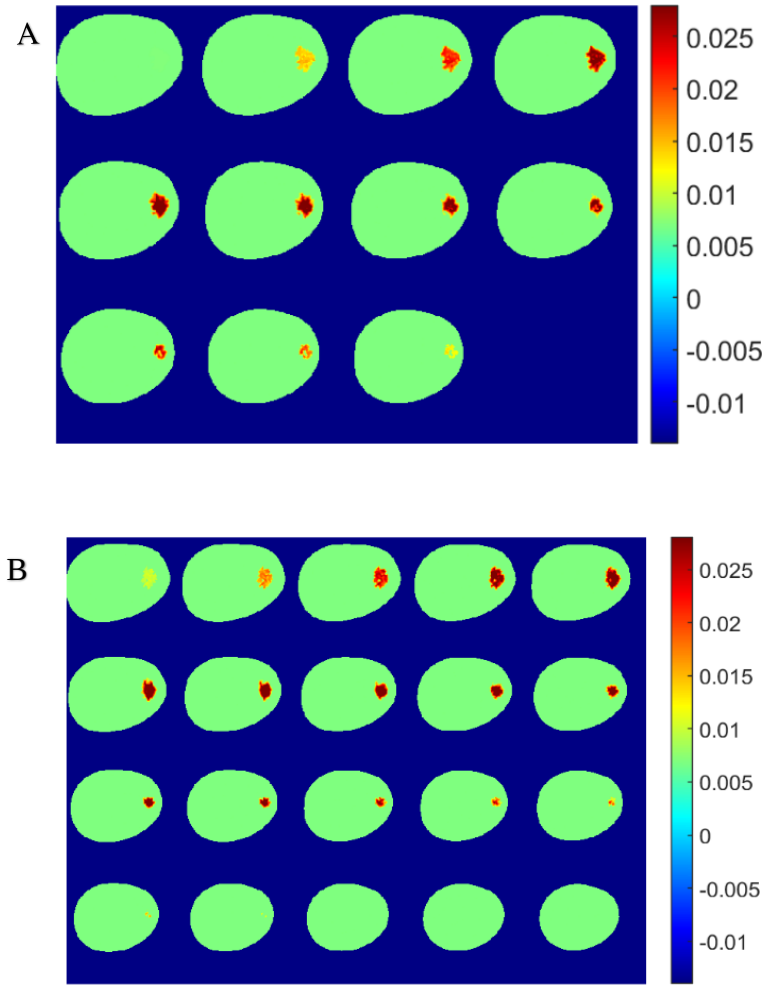

Figure 2.14: Absorption coefficient plot. (A) case 1. (B) case 2.

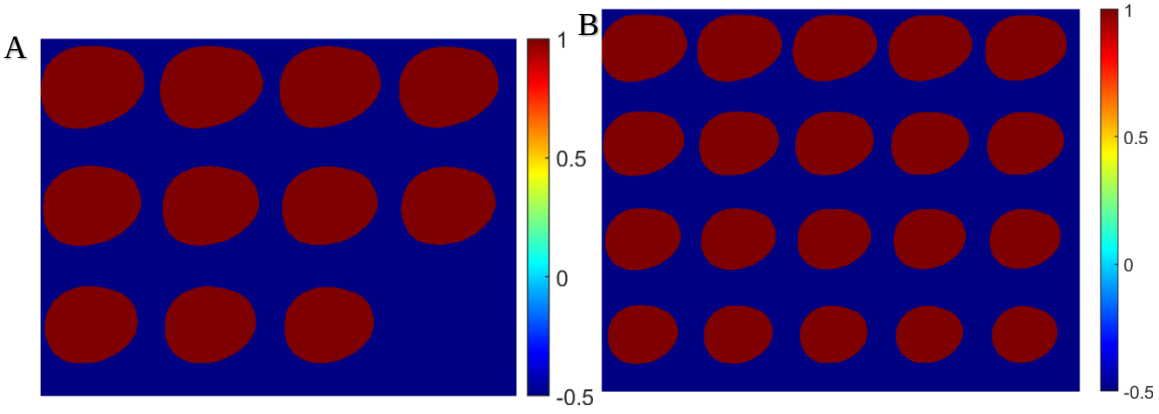

Figure 2.15: Reduced scattering coefficient plot (A) Case 1. (B) Case 2.

2.4.5 Phi

Phi represents the calculated photon density distributed inside the three – dimensional (3D) object and is defined on each node of the finite element mesh. The phi values on the surface can be the numerical measurement depending on the definition of the detector nodes. For example, in the ring based set up, a single source position is turned on and then all 10 detectors are turned on and collect photons on their corresponding detector nodes, which are then stored as measured values for the forward modeling and the reconstruction. Figure 2.16 shows the images of the calculated photons collected when a specific source position is turned on, where the dark red region indicates the source position and the color bar scale indicates the calculated phi.

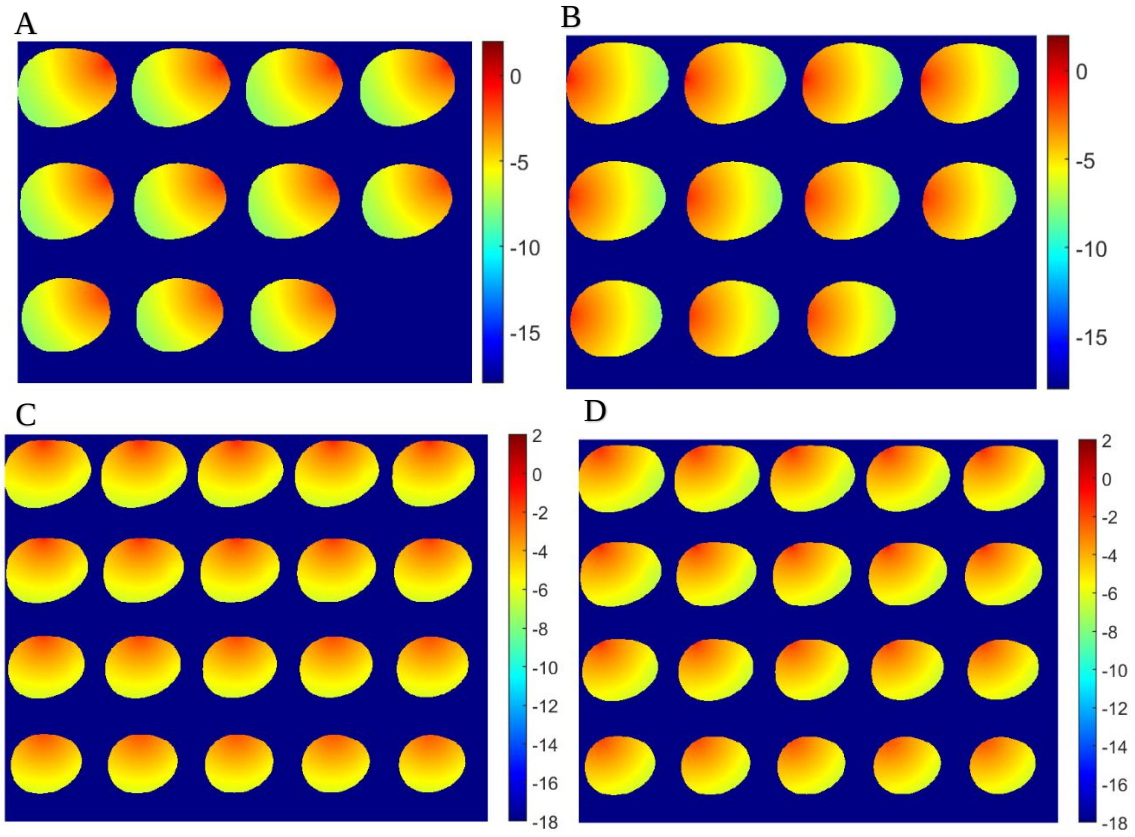

Figure 2.16: Calculated images of Phi. (A) Mesh case 1 for source point 11. (B) Mesh case 1 for source point 12. (C) Mesh case 2 for source point 11. (D) Mesh case 2 for source point 1. Note: the color bar is at a logarithmic scale.

2.5 Experimental Schematic Drawings

This section provides two brief experimental schematic drawings for the ring based and camera-based detector system. The ring detector set up involves evenly spaced detectors and sources placed around the breast. As each source is turned on then all the detectors turn on. Then the ring can be shifted up or down or right or left depending on where the next source position is desired. See Figure 2.17 below to see the ring based detector set up.

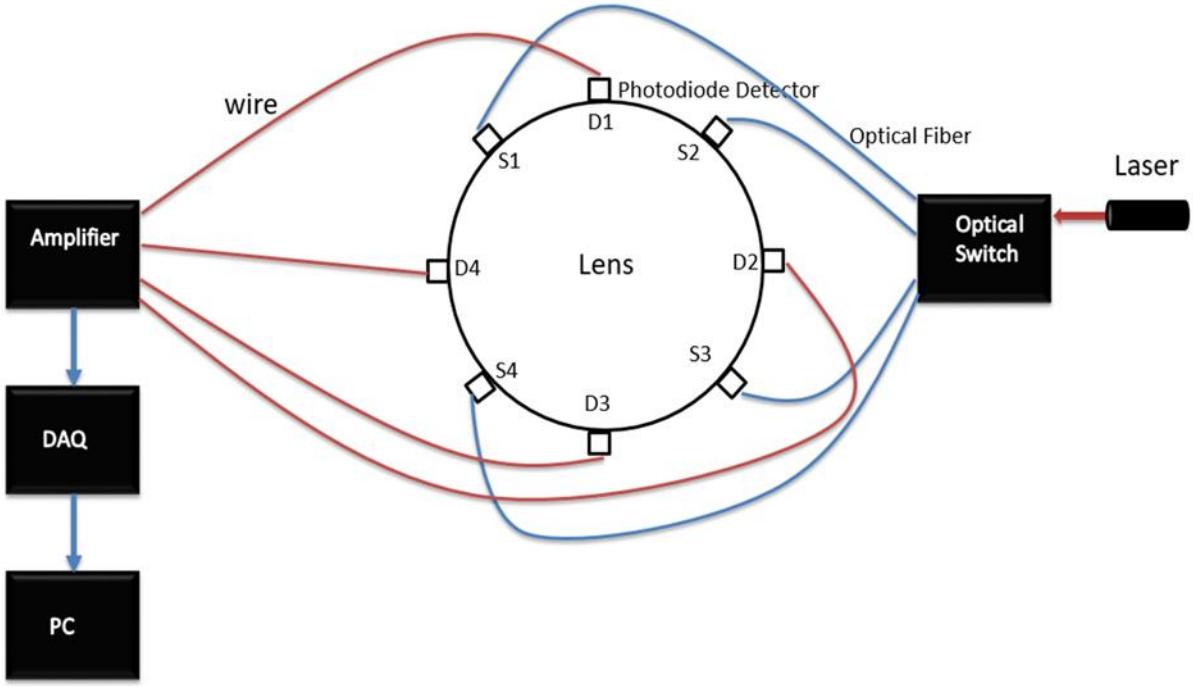

Figure 2.17: Ring detector set up.

In Figure 2.17, four detectors and four sources are seen equally spaced. Note that in this study 10 detectors were simulated per source. Since the breast is not a defined geometric shape, there were only 9 detectors simulated to be turned on per source towards the outward surfaces of the breast. This detector set up is cost effective in that the optical switch allows different detectors to be used for multiple acquisitions. The random based detector set up is not pictured because it is very similar to the ring-based detector set up. However, in random based detector set up, the detectors are placed over the whole breast surface for each source position, which represents the best scenario case in terms of measurements.

The next experimental schematic drawing presented is the PET/CT guided DOT camera-based system. See Figure 2.18 below.

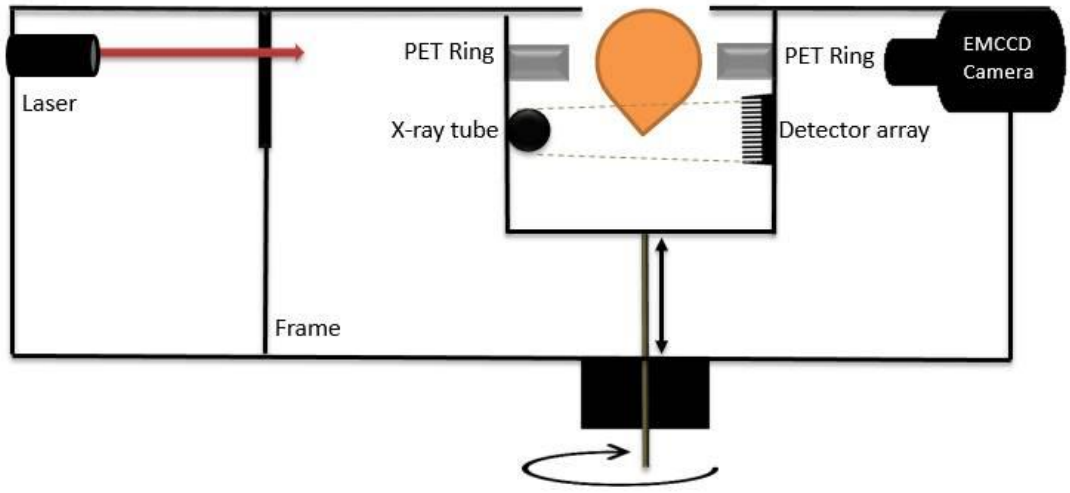

Figure 2.18: PET/CT guided DOT camera based imaging system's experimental schematic drawing.

In Figure 2.18, there is an x-ray tube for the CT imaging system. The dotted lines represent the field of measurement. There is also an anti – scatter collimator on top of the detector array. The CT system will take the CT scans for the structural prior information for the DOT image reconstruction. There are also PET rings placed around the breast. These PET rings will detect the gamma rays that are emitted during imaging. These PET rings will be able to move up and down along the breast surface. After the PET ring is moved down, the whole system will move around the breast surface to allow for multiple DOT acquisitions with the EMCCD camera.

2.6 Conclusions

In summary, breast CT and breast PET images were used to construct 3D breast models. Two different breast mesh cases were compared from the generated 3D breast models. Three different detector based set ups were created for each of the two breast mesh cases. The breast and breast tumor were assigned optical properties. Then, the absorption and optical properties were plotted based on the defined values. Finally, the measurements were obtained for both breast mesh cases. This chapter concluded by providing a visualization of the ring based and camera-based detector systems simulated in this study. The reconstruction results from Chapter 3 will provide insight to the feasibility of the detector based setups based on the quality of the reconstructed images.

Chapter 3

Reconstruction Results

3.1 Introduction

Chapter 3 provides the reconstruction results using the numerical measurements from the forward modeling and the detector setups as described in Chapter 2. In Chapter 2, the optical properties of the breast and breast tumor were defined. Then, measurements or photon propagation information was obtained based on the source/detector configurations. In Chapter 3, the DOT inverse problem is solved by updating the absorption coefficient at each node in the two different mesh cases. The equations used for the reconstruction are explained in section 1.2.4 of Chapter 1. DOT is ill – posed so regularization methods are used in the reconstruction. The first step is iterative minimization of the quadratic error between the modeled and measured data [24]. The Jacobian, or sensitivity matrix, is updated after each iteration. There is an update after each iteration of difference between the measured and calculated data. This updating equation or the Levenberg – Marquardt algorithm is based on the nonlinear Newton iterative method [25] [26] [27]. When convergence occurs, the solution is accepted [22]. The output is used to map the reconstructed optical properties. There has been extensive research done on different types of regularization methods for image reconstruction. The typical image reconstruction approach used in this study is the Tikhonov-type regularization [54]. This regularization imposes restrictions on the absorption and the reduced scattering coefficients. It works best when the unknown optical properties follow a Gaussian distribution. This type of regularization provides a clear image of optical properties [54].

This chapter presents multiple reconstruction results with the different mesh cases and various detector setups as described in Chapter 2. The results with noise are also presented. The purpose of Chapter 3 is to use the reconstruction results to validate the feasibility of the design and optimization of the optical detectors and laser sources for a future physical PET/CT guided DOT imaging system

3.2 Soft Prior Reconstruction

3.2.1 Structural prior

As previously mentioned, diffuse optical tomography uses light in the wavelength range from 650 to 900 nm to recover images of the internal distribution of breast tissue optical properties due to the high penetration power of optical photons in these wavelengths. These measurements can be used to estimate the tissue hemoglobin and water concentrations using no ionizing radiation and no invasive techniques. However,

DOT is a nonlinear, ill-posed and ill-conditioned problem. Incorporation of structural prior information, specifically CT derived breast geometry, can help improve the quantitative accuracy of the reconstructed DOT images. By knowing the exact location of the spatial distribution of the optical properties, breast tumor information can be obtained. Therefore, therapeutic monitoring can also be done by monitoring the change of tumor optical properties.

Structural prior information can help improve the low spatial resolution issues DOT poses. A known method of introducing structural prior information is the incorporation of hard-priors. In this method the mesh of the 3D object is segmented and all nodes within each region are assigned the respective optical properties [55]. The optical properties in the same region must be uniform [40]. This method involves the reduction of the number of unknown parameters to be estimated. Some issues presented are introducing error by incorrect model assumptions and uncertainty in the prior information [56]. The co-registration between the DOT imaging system and the one used to obtain the structural prior information may not be accurate. Segmentation of the 3D object may also introduce classification errors due to digitization [56].

The soft prior method has since then been introduced to improve upon the issues the hard prior method presents. The soft prior method allows for smooth changes of the reconstructed optical properties in various regions [40]. In section 1.2.4 the equations for the soft prior method of incorporation of structural priors are described. The λ variable in equation 1.6 is the specific regularization parameter that balances the estimate between the optical properties and initial values and the data – model misfit [56]. This variable is particularly tuned when implementing noise in the reconstruction in this study. The L variable in equation 1.6 contains the matrix that is obtained from structural imaging modalities such as CT in this study. The L matrix is a penalty matrix where it is dimensionless in all cases. It relates each nodal property of the numerical model to all other modes within the mesh [56]. The soft prior method doesn't require the property estimates in a specific region to be constant [57]. It uses the boundary data to preserve the property changes with different tissues. It specifically encodes spatial information into a matrix that associates points in the same region to minimize variation within different breast regions [57]. The soft prior method in this study used for reconstruction to prove the feasibility of the PET/CT guided DOT imaging system. Results with noises are also presented to further draw upon the implications.

3.2.2 Noise

To validate feasibility of a PET/CT guided DOT imaging system, reconstruction results are also presented with noises. The purpose is to examine whether results obtained with noise continue to show positive implications. The results are presented with 1% noise for the different mesh cases and the three different detector set ups respectively. Then the ring detector setup is chosen to be simulated with 1%,2% and 5% noise.

Noise is normally seen as undesired disturbance in the electrical signal or disturbance during acquisition of important information. The source of noise in the system may be electrical or optical. The noise may come from electrical power grounding, fluctuation of power supply, electromagnetic disturbance, digital grounding of computer, preamplifier in photodiodes, operations amplifier offset and resistance variation in resistors [17]. Optical noises from laser modules may also be present. The EMCCD camera or the photodiode detectors may also produce slight electrical variations leading to noise. Thermal noise, or white noise, or Johnson – Nyquist noise, is generated by variation of electrons in an electrical conductor at equilibrium [58]. This type of distribution is implemented in the reconstruction.

3.2.3 Artifacts and background in DOT imaging

DOT imaging can be deteriorated by not only noise but also by artifacts. Artifacts are similar to noise. However, they are caused by errors such as computational, modeling and detector/source fiber coupling errors [30]. They can show up in different patterns and range in sizes. Artifacts in DOT imaging can result in unnecessary biopsies for patients [30].

DOT has low spatial resolution and lesion uncertainty can be caused by light scattering in soft breast tissue [59]. This can make distinguishing the background healthy breast tissue, benign lesions and malignant lesions difficult. Clinical studies have shown that tumorous tissues have higher hemoglobin concentrations [59]. To overcome the lesion uncertainty, multi-channel data acquisition system can be implemented to obtain measurements at different wavelengths to allow for hemoglobin, water and lipid chromophore concentration information to be obtained. Furthermore, studies have been done for over 10 years in which DOT has been guided by mammography, ultrasound and MRI to improve the light quantification accuracy and spatial resolution of DOT images [59]. It is believed that the PET/CT guided DOT system analyzed in this study will prove to provide robust images with good quantitative accuracy.

3.3 Reconstruction Results

This section will provide the reconstruction results based on the mesh cases and the different detector-based set ups that were simulated in this study. The reconstructions results were obtained after 5 iterations. The initial u_a value from the forward modeling was used as the final u_a for the reconstruction.

3.3.1 DOT reconstruction with two different meshes

This subsection compares the reconstruction results for the two mesh cases. The detector set up is the random based. Both mesh cases have 1% noise added onto the numerical measurements. Figures 3.1 and Figure 3.2 plot the reconstructed absorption coefficient images at different slices for the mesh case 1 and case 2, respectively. In both figures the slices of the reconstructed absorption coefficient images are plotted with a color bar where the tumor is indicated by the red color due to its high contrast to the background. For both cases, the tumor has been reconstructed successfully at the right locations with good quantitative accuracy. The tumor is more thoroughly seen in mesh case 2 because of the greater number of layers compared to mesh case 1.

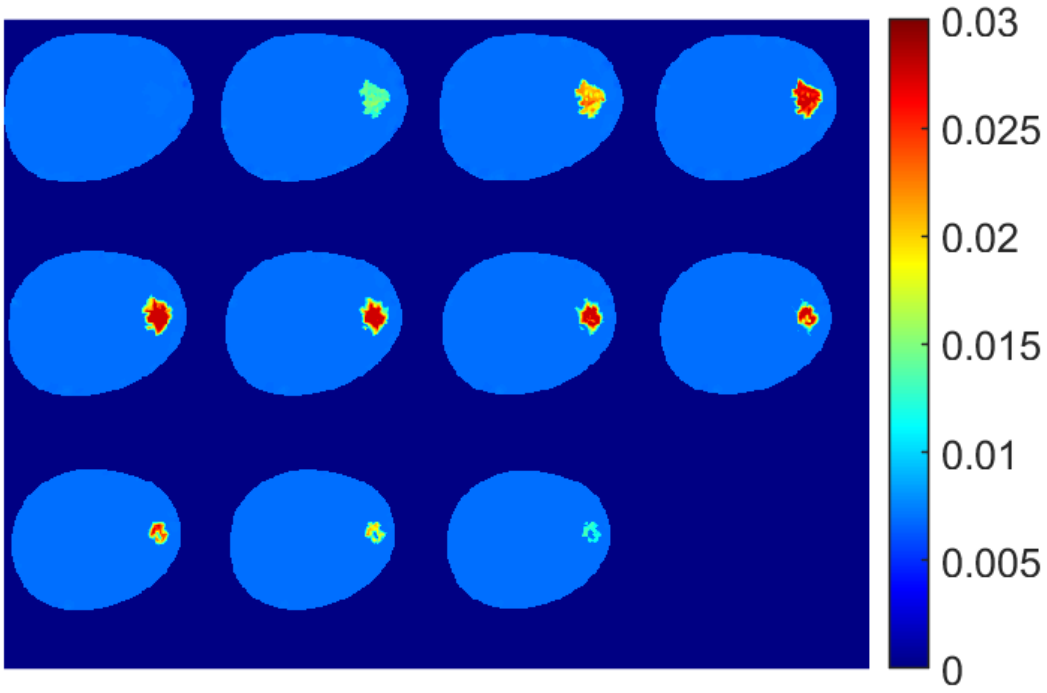

Figure 3.1: Images of the reconstructed absorption coefficients for mesh comparison: case 1 with 1% noise added.

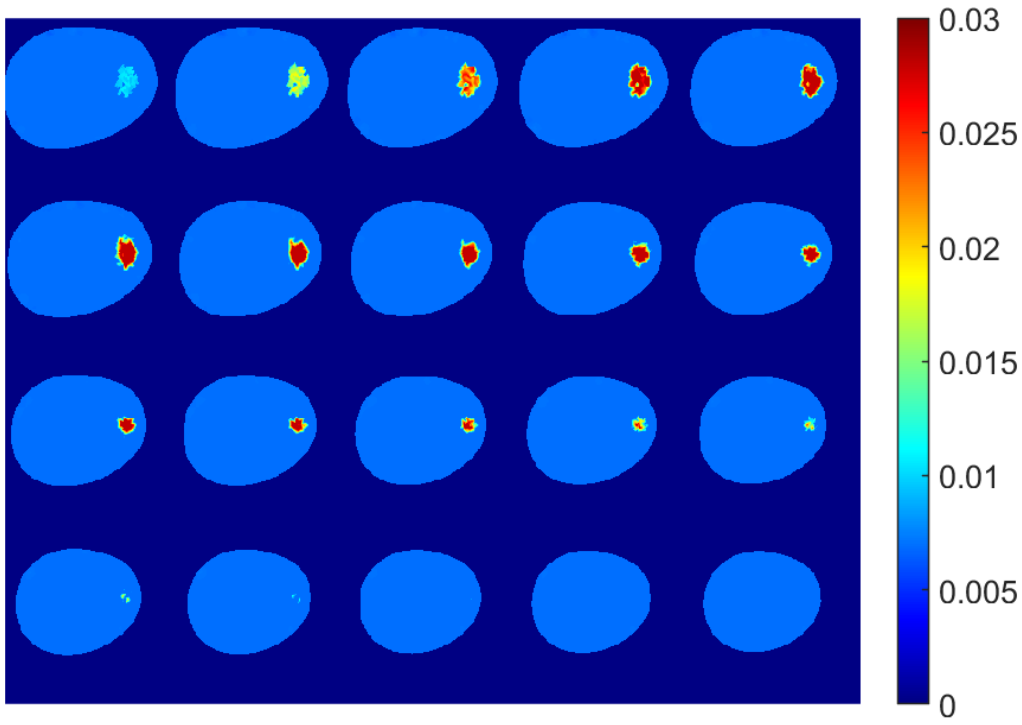

Figure 3.2: Images of the reconstructed absorption coefficients for mesh comparison: case 2 with 1% noise added.

3.3.2 DOT reconstruction with different detector set ups

This subsection compares the reconstructed absorption coefficient images for the different detector setups using mesh case 1. There is 1% noise presented in all the reconstructions. Figures 3.3,3.4 and 3.5 plot the reconstructed absorption coefficient images for random based detectors, ring based detectors and camera based detectors, respectively. From these images, it is seen that all absorption coefficient images have been reconstructed very well.

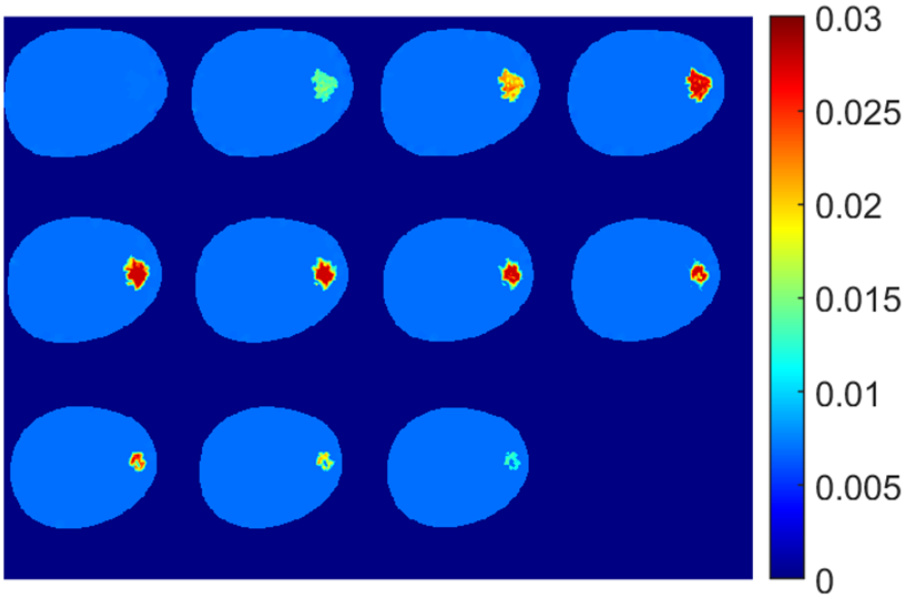

Figure 3.3: Images of the reconstructed absorption coefficients for the random detector based set up in mesh case 1 with 1% noise added.

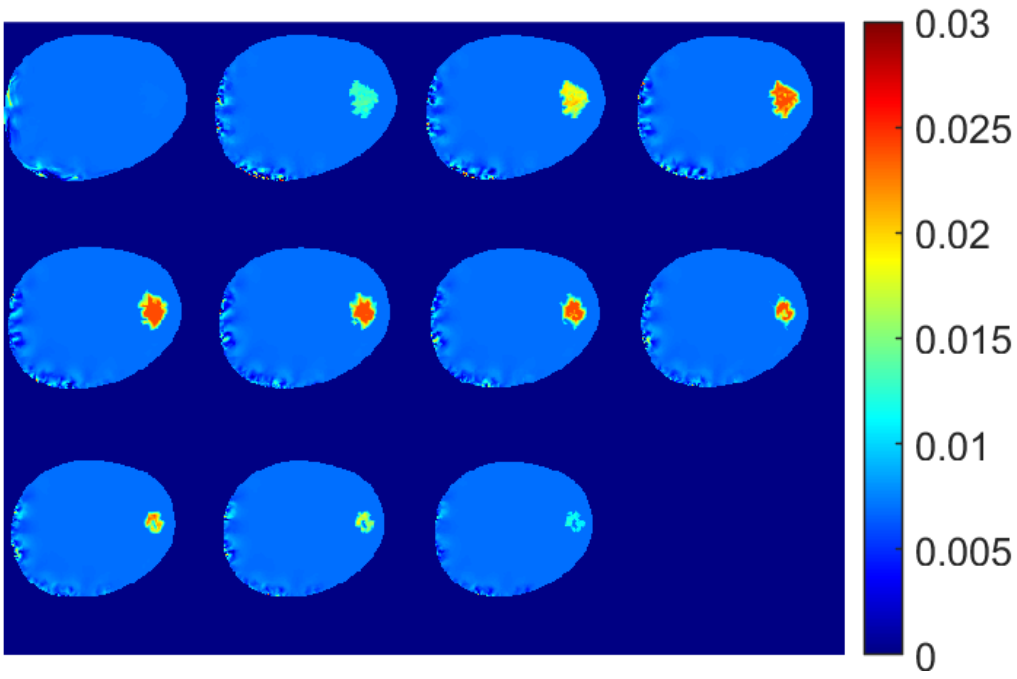

Figure 3.4: Images of the reconstructed absorption coefficients for the camera detector based set up in mesh case 1 with 1% noise added.

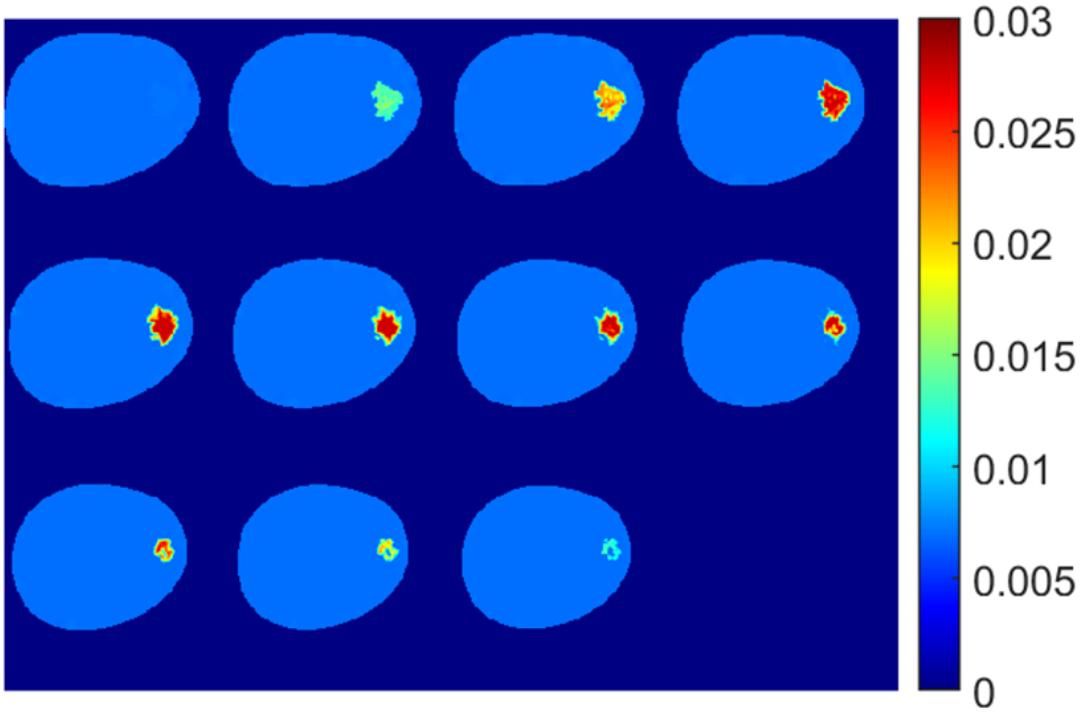

Figure 3.5: Images of the reconstructed absorption coefficients for the ring detector based set up in mesh case 1 with 1% noise added.

The next two graphs compare the profile plots of the ground truth with the reconstruction results. The purpose of the graphs is to further analyze which detector method provides the best reconstruction. The intensity values were extracted along the breast surface and the tumor. These intensity values were then plotted against the size of the breast. Figure 3.6 is plotted below, from which we see that the tumor is reconstructed at the right locations for all three detector setups.

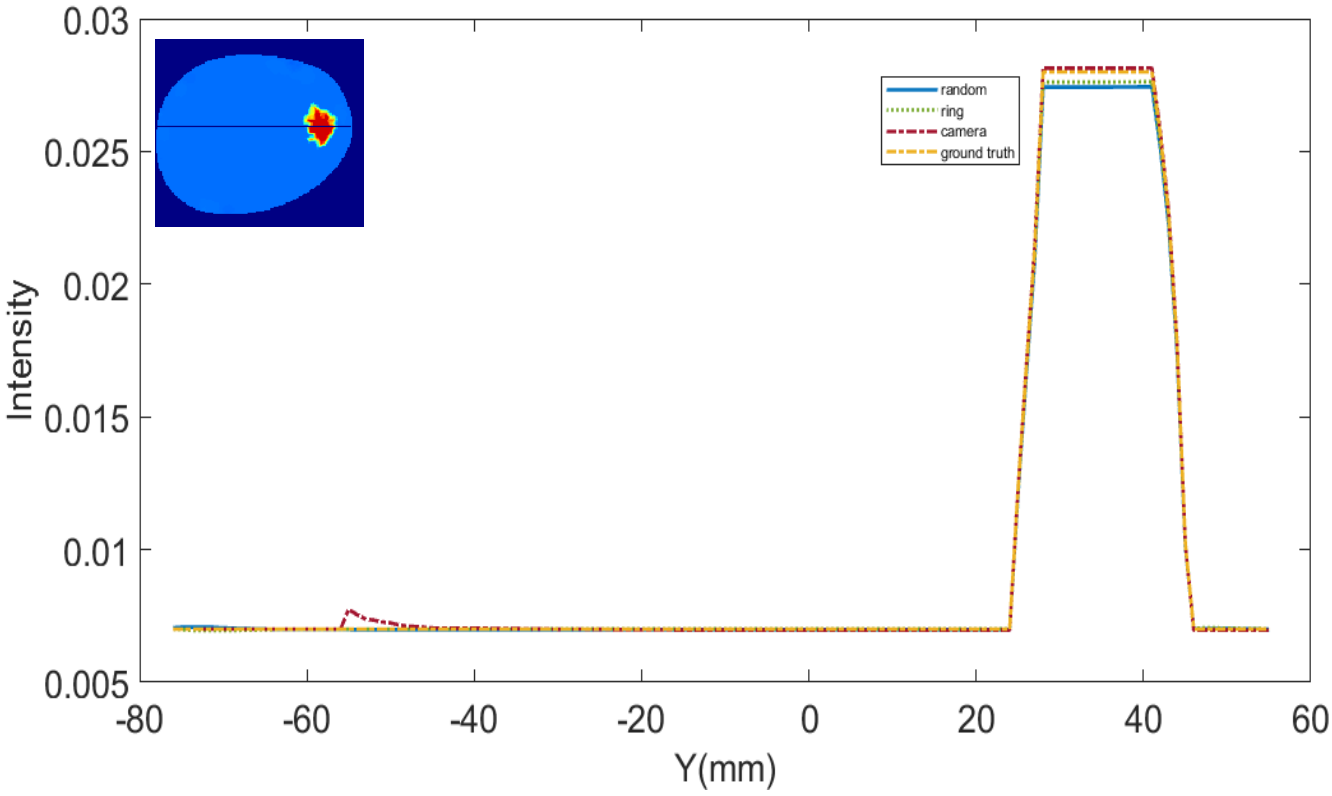

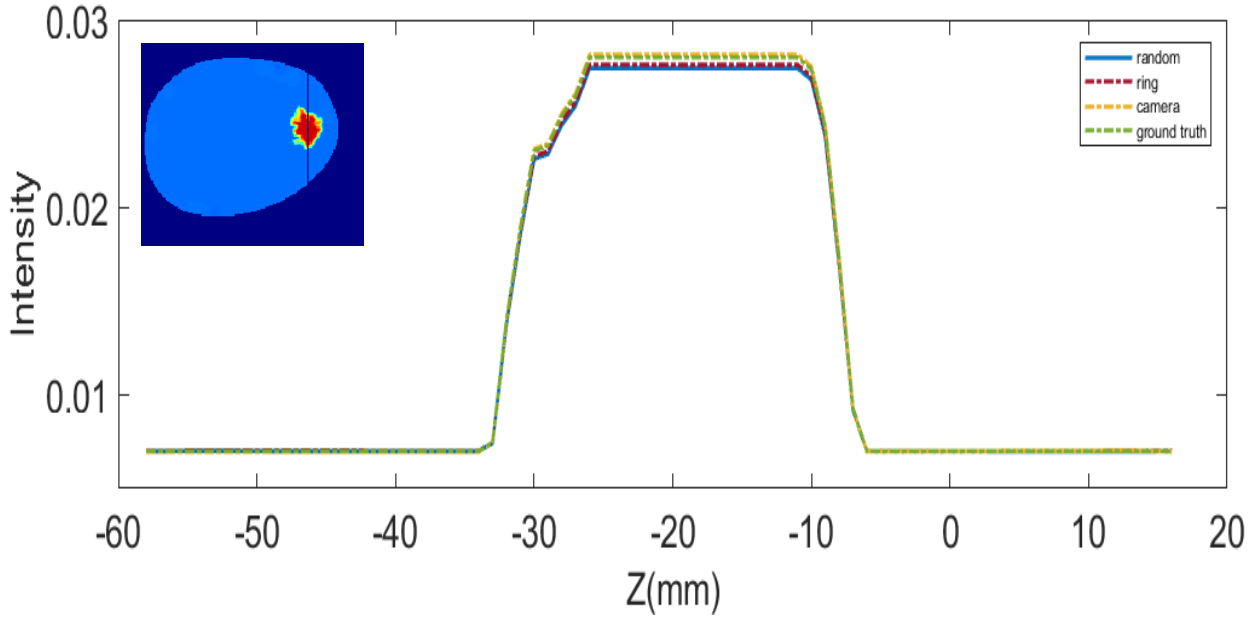

Figure 3.6: Profile plots of ground truth with reconstruction results for different detector setups. (A) Profile plot when y = 60 (B) Profile plot when x = 116.

The following tables are the extracted values of the peaks of the graphs presented in Figure 3.6. The tables also present the % error between the peak values of the ground truth and the reconstruction results. The purpose of comparing the peak values is to further analyze which detector method best matched the ground truth.

Table 3.1: Profile analysis table for target peak of reconstruction results for different detector setups.

	Ground truth	Random	Ring	Camera
Target peak (Y)	0.028	0.0274	0.0276	0.0283
% error		2.14	1.42	1.07

	Ground truth	Random	Ring	Camera
Target peak (Z)	0.028	0.0274	0.0276	0.0281
% error		2.14	1.42	0.3

Based on the peak values seen in Table 3.1 and the graphs in Figure 3.6, it can be confirmed that the ring based detector system provides the most similar reconstruction result to the ground truth, while the camera based detector setup has slightly better accuracy than the other two detector setups.

This conclusion is confirmed by further image analysis. The metrics measured include: volume ratio (VR), dice similarity coefficient (Dice), mean squared error (MSE) and contrast-to-noise ratio (CNR). VR measures the sparsity of the reconstructed target, Dice quantifies the shape and location accuracy, MSE is the error between the ground truth and reconstruction and CNR is for the reconstructed image [60]. Their definitions represented below [60]:

$$\text{VR} = \frac{|ROI|}{|tROI|} \tag{3.1}$$

$$\text{DICE} = \frac{2*|ROI \cap tROI|}{|ROI|+|tROI|} \tag{3.2}$$

$$\text{MSE} = \frac{1}{N}\sum_{j=1}^{N}(x_j - x_{0j})^2 \tag{3.3}$$

$$\text{CNR} = \frac{Mean(x_{ROI}) - Mean(x_{ROB})}{\sqrt{\omega_{ROI} Var(x_{ROI}) + (1-\omega_{ROI}) Var(x_{ROB})}} \tag{3.4}$$

where *ROI* is the region of interest, *ROB* are the other voxels, *tROI* are the true target locations, x is the reconstructed image intensity and x_0 is the true image intensity and ω_{ROI} = |*ROI*|/|Total image| [60]. The values obtained from the metrics calculations for the different detector setups are represented in Table 3.2 below.

Table 3.2: Metrics analysis table of reconstruction results for different detector setups.

	DICE	VR	CNR	MSE
Random	1.0	0.99	18.24	2.35×10^{-5}
Ring	1.0	0.99	18.25	1.30×10^{-5}
Camera	30	0.06	4.26	0.37

The ideal metric values are defined as having Dice and VR be closest to 1, the CNR be large and the MSE be small [60]. The ring-based detector set up seems to most closely match the ideal values when compared against the random based and camera based set up. Based on the analysis of the results, the ring based detector set up is then chosen to be analyzed with various levels of noise in the next subsection.

3.3.3 DOT reconstruction with different noise levels

This subsection compares the reconstruction results for the ring-based detector setup using case 1 with 0%,1%,2% and 5% noise levels. The purpose of comparing with different levels of noise is to confirm that even with varying levels of noise present in the hardware there still can be good reconstruction results obtained. See Figures 3.7, 3.8, 3.9 and 3.10 below.

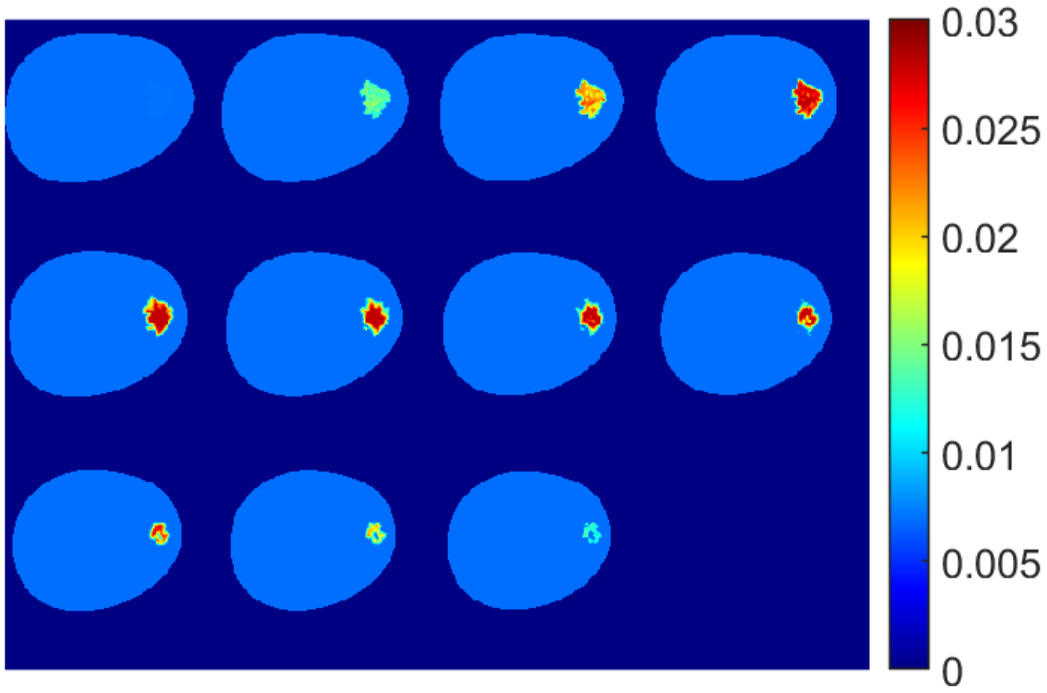

Figure 3.7: Images of the reconstructed absorption coefficients for 0% noise.

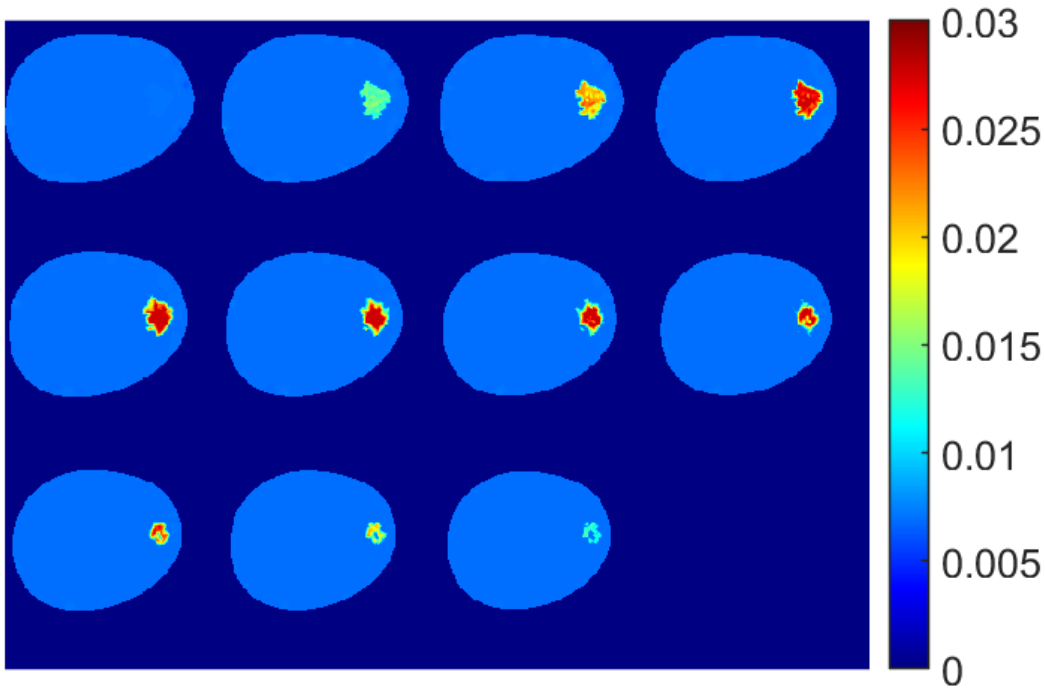

Figure 3.8: Images of the reconstructed absorption coefficients with 1% noise added.

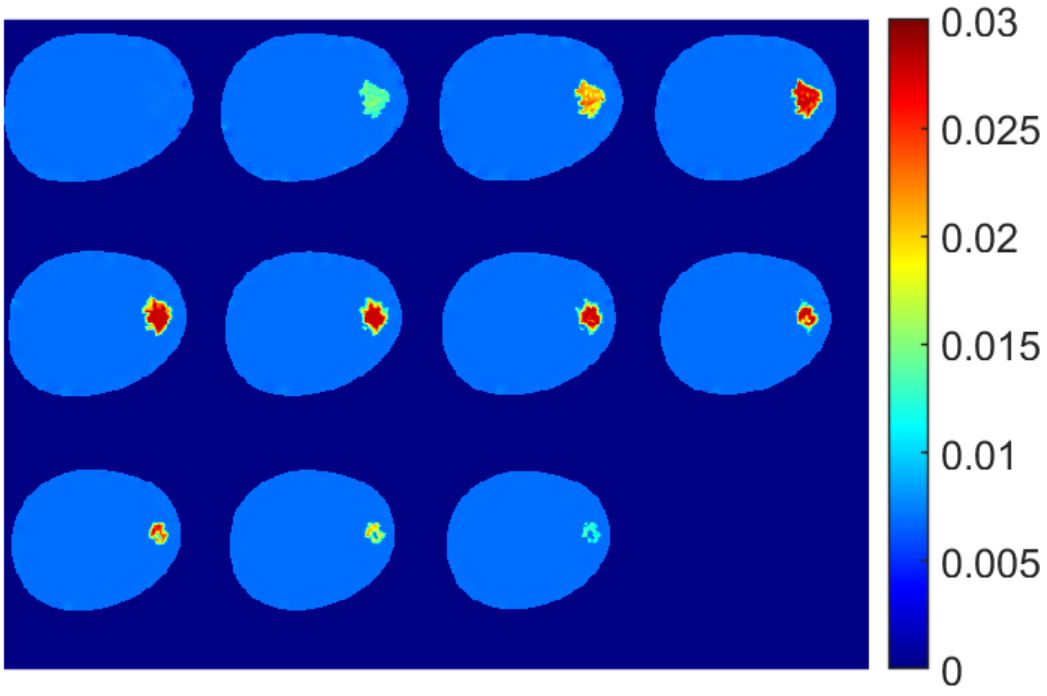

Figure 3.9: Images of the reconstructed absorption coefficients with 2% noise added.

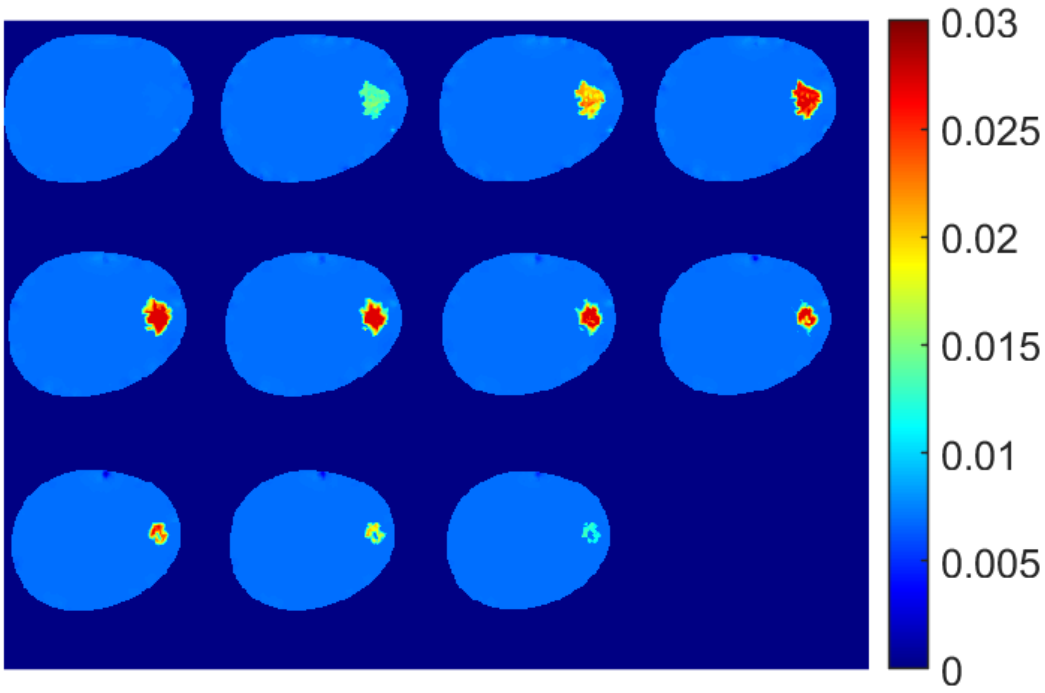

Figure 3.10: Images of the reconstructed absorption coefficients with 5% noise added.

The next two graphs compare the profile plots of the ground truth with the reconstruction results of the ring based detector system with varying levels of noise. These graphs were generated similarly to the graphs in Figure 3.6.

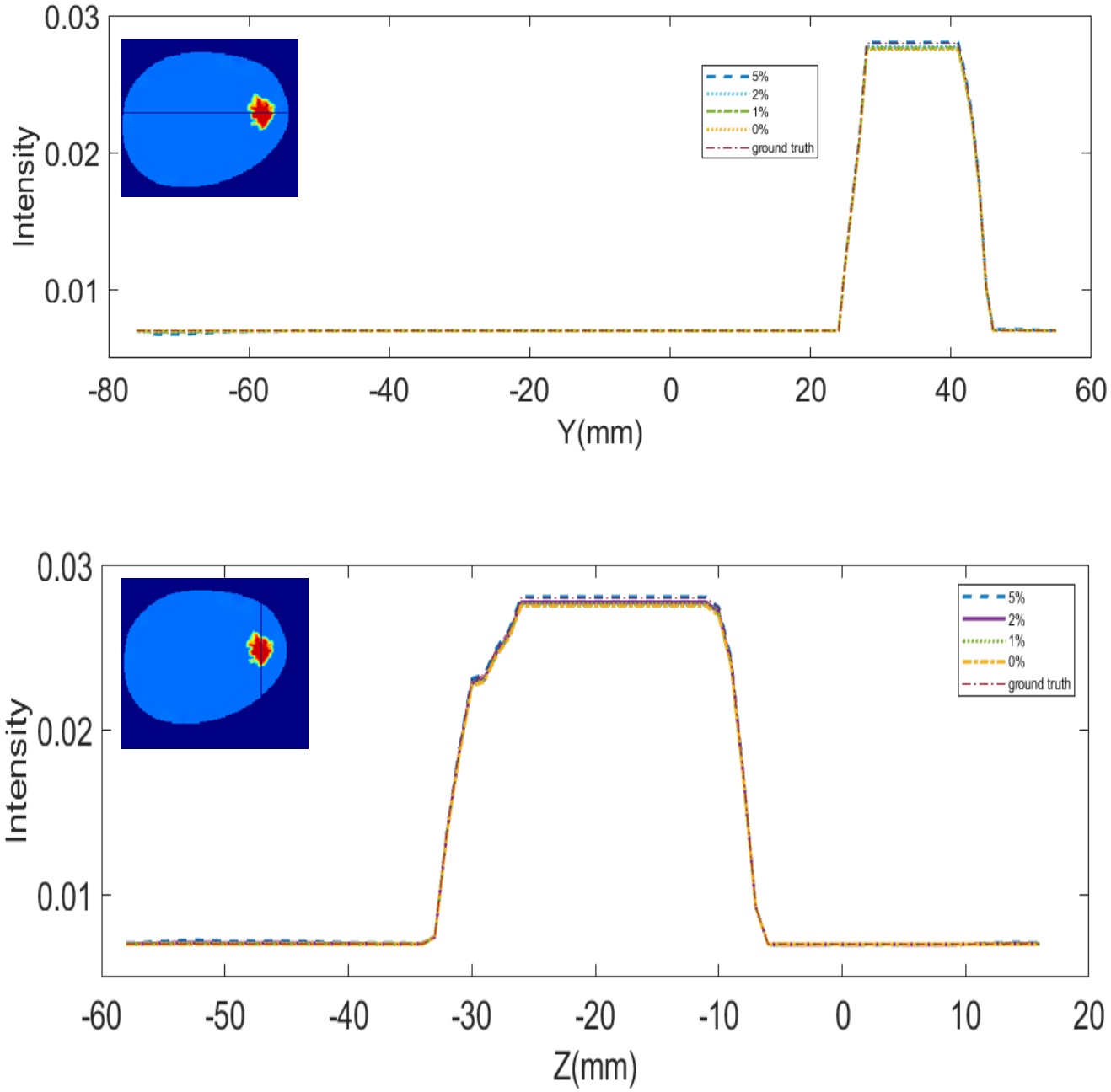

Figure 3.11: Profile plots of ground truth and the reconstruction results with different noise levels for ring-based detector set up: (A) Profile plot when y = 60 (B) Profile plot when x = 116.

The following tables in Table 3.3 contain the extracted values of the peaks of the graphs presented in Figure 3.11. The tables also present the % error between the peak values of the ground truth and the reconstruction results. The purpose of comparing the peak values is to further analyze how the reconstruction results compare to the ground truth with varying levels of noise. The results confirm that DOT reconstruction with soft prior guidance is robust to the noises up to 5%.

Table 3.3: Profile analysis table for target peak of reconstruction results with varying noise levels for ring-based detector set up.

	Ground truth	0%	1%	2%	5%
Target peak (Y)	0.028	0.0275	0.0276	0.0277	0.0281
% error		1.78	1.42	1.07	0.35

	Ground truth	0%	1%	2%	5%
Target peak (Z)	0.028	0.0275	0.0276	0.0277	0.0280
% error		1.78	1.42	1.07	0

The conclusion that the ring-based detector setup produced reconstruction results robust to noises up to 5% are confirmed by further image analysis. The metrics measured include: volume ratio (VR), dice similarity coefficient (Dice), mean squared error (MSE) and contrast-to-noise ratio (CNR). The values obtained from the metrics calculations for the different noise levels are represented in Table 3.4 below.

Table 3.4: Metrics analysis table for reconstruction results with varying noise levels for the ring-based detector set up.

	DICE	VR	CNR	MSE
0%	1.0	0.99	18.25	1.91×10^{-5}
1%	1.0	0.99	18.25	1.30×10^{-5}
2%	1.0	0.99	18.22	1.08×10^{-5}
5%	1.0	1.0	18.20	2.65×10^{-5}

The ideal metric values are defined as having Dice and VR be closest to 1, the CNR be large and the MSE be small [60]. Based on the results in Table 3.4, the ring-based detector setup is confirmed to be robust to varying levels of noise.

3.4 Discussions and Conclusions

The first reconstruction results obtained were comparing the two mesh cases. Figure 3.2 showed the tumor more spread out along the breast surface. With a larger mesh the tumor has a better presence. However, a larger mesh results to longer computation time. Keeping this in mind the reconstruction for analyzing the different detector setups were done with mesh case 1. Figure 3.5, Figure 3.6 and Table 3.1 showed implications all three detector cases have obtained similar reconstruction results, which implied that the ring based detector setup is feasible and most cost effective. It does not require the purchase of many different detectors like in the random based detector set up. To further confirm these results the ring based detector set up was used in the noise analysis. After reconstructing with varying levels of noise the ring based detector set up still showed almost same peak values compared to the ground truth. As mentioned in section 3.2.2 noise is a very common during acquisition and imaging. By simulating good results with noises, it can be seen that the ring based detector set up provides positive implications

Chapter 4

Conclusion and Future Work

In this present work, the feasibility of a PET/CT guided DOT imaging method and system build for breast cancer imaging was studied. The finite element mesh method was used to create two different breast mesh models. These models were used to solve the diffuse equation to simulate DOT imaging. The breast meshes were generated from breast CT images. An edge detection method was implemented to extract the breast shape from the CT images to generate a 3D breast mesh model. This algorithm developed may be used for extracting other organs from CT images. The real tumor location was obtained based on prior information from PET images. Three different detector set ups including ring based, random based and camera based were compared. Experimental schematic drawings for the ring based and camera based detector set up were presented. The reconstruction results from comparing the different detector set ups proved the ring based detector to be the most optimal.

The ring based detector set up provided similar results compared with the random detector case and the camera detector case. This set up will be the most cost effective and time saving with good results. The ring based detector set up was further analyzed with varying noise levels. The reconstruction results and analysis proved the set up to provide good results with varying noise levels. The reconstruction results validate the feasibility of the design and optimization of the optical detectors and laser sources for a future PET/CT guided DOT imaging system.

In the future, a PET/CT guided DOT imaging system with ring based silicon photodiodes will be implemented. This imaging system will contain 10 silicon photodiodes and 4 continuous wave lasers at different wavelengths for multispectral measurements. The use of 4 continuous wave lasers at different wavelengths are chosen because of the goal of obtaining information regarding 4 different unknowns during DOT imaging. These unknowns include: deoxyhemoglobin, oxyhemoglobin, water and lipid. The system will further be controlled by an optical switch to allow for multiplexing of the detectors. The ring will rotate around and move up and down along the breast surface. This will allow for multiple acquisitions with no need of more detectors. This will also allow for more measurement data, which will make it possible to reconstruct reduced scattering coefficients with optical absorption coefficients. This will also allow the possibility of monitoring changes in hemoglobin concentrations and oxygenation specifically during neoadjuvant chemotherapy.

References

[1] (). *U.S. Breast Cancer Statistics*. Available: http://www.breastcancer.org/symptoms/understand_bc/statistics.

[2] Janet R. Osuch *et al*, "A Historical Perspective on Breast Cancer Activism in the United States: From Education and Support to Partnership in Scientific Research," *J Womens Health (Larchmt)*, vol. 21, pp. 355-362, 2012. Available: https://www.ncbi.nlm.nih.gov/pmc/articles/PMC3298674/. DOI: 10.1089/jwh.2011.2862.

[3] Perkins C. Morris C. Wright W., "Cancer Incidence And Mortality in California by Race/Ethnicity," *Sacramento, CA: California Department of Health Services, Cancer Surveillance Section*, vol. 1996, 1993. Available: http://www.ccrcal.org/PDF/Regional_Registries/Reg4AnnualReport-1988-2005.pdf.

[4] B. Zhang *et al*, "Guidelines on the diagnosis and treatment of breast cancer (2011 edition)," *Gland Surgery*, vol. 1, *(1)*, pp. 39, 2012. Available: http://www.ncbi.nlm.nih.gov/pubmed/25083426.

[5] (). *What Is Breast Cancer?*. Available: https://www.cancer.org/cancer/breast-cancer/about/what-is-breast-cancer.html.

[6] "Screening for Breast Cancer: U.S. Preventive Services Task Force Recommendation Statement," *From the U.S. Preventive Services Task Force, Agency for Healthcare Research and Quality, Rockville, Maryland*, Available: http://annals.org/aim/fullarticle/745237/screening-breast-cancer-u-s-preventive-services-task-force-recommendation.

[7] Norman F Boyd, Lisa J Martin, Martin J Yaffe, Salomon Minkin, "Mammographic density and breast cancer risk: current understanding and future prospects," *Breast Cancer Research*, vol. 13, *(6)*, pp. 1, Available: https://breast-cancer-research.biomedcentral.com/articles/10.1186/bcr2942.

[8] S. H. Heywang-Köbrunner, A. Hacker and S. Sedlacek, "Advantages and Disadvantages of Mammography Screening," *Breast Care*, vol. 6, *(3)*, pp. 199-207, 2011. Available: https://www.karger.com/Article/Abstract/329005. DOI: 10.1159/000329005.

[9] D. Saslow *et al*, "American Cancer Society guidelines for breast screening with MRI as an adjunct to mammography," *CA Cancer J Clin*, vol. 57, *(2)*, pp. 75-89, 2007.

[10] Rakesh Kumar *et al*, "Clinicopathologic factors associated with false negative FDG–PET in primary breast cancer," *Breast Cancer Res Treat*, vol. 98, *(3)*, pp. 267-274, 2006. Available: https://link.springer.com/article/10.1007/s10549-006-9159-2. DOI: 10.1007/s10549-006-9159-2.

[11] Eric L. Rosen, MD, William B. Eubank, MD, and David A. Mankoff, MD, PhD, "FDG PET, PET/CT, and Breast Cancer Imaging," *RadioGraphics,* vol. 27, *(1),* 2007. Available: https://pubs.rsna.org/doi/abs/10.1148/rg.27si075517.

[12] J. Ruiz *et al*, "Breast density quantification using structured-light-based diffuse optical tomography simulations," *Appl. Opt. , AO,* vol. 56, *(25),* pp. 7146-7157, 2017. Available: https://www.osapublishing.org/ao/abstract.cfm?uri=ao-56-25-7146. DOI: 10.1364/AO.56.007146.

[13] R. Choe *et al*, "Diffuse optical tomography of breast cancer during neoadjuvant chemotherapy: a case study with comparison to MRI," *Med Phys,* vol. 32, *(4),* pp. 1128-1139, 2005. . DOI: 10.1118/1.1869612.

[14] D. R. Leff *et al*, "Diffuse optical imaging of the healthy and diseased breast: a systematic review," *Breast Cancer Res. Treat.,* vol. 108, *(1),* pp. 9-22, 2008. . DOI: 10.1007/s10549-007-9582-z.

[15] E. A. Lim *et al*, "Diffuse optical tomography changes correlate with residual cancer burden after neoadjuvant chemotherapy in breast cancer patients," *Breast Cancer Res. Treat.,* vol. 162, *(3),* pp. 533-540, 2017. . DOI: 10.1007/s10549-017-4150-7.

[16] C. Jacquillat *et al*, "Results of neoadjuvant chemotherapy and radiation therapy in the breast-conserving treatment of 250 patients with all stages of infiltrative breast cancer," *Cancer,* vol. 66, *(1),* pp. 119-129, 1990.

[17] C. Li *et al*, "Multispectral breast imaging using a ten-wavelength, 64 x 64 source/detector channels silicon photodiode-based diffuse optical tomography system," *Med Phys,* vol. 33, *(3),* pp. 627-636, 2006. . DOI: 10.1118/1.2171508.

[18] J. P. Culver *et al*, "Three-dimensional diffuse optical tomography in the parallel plane transmission geometry: evaluation of a hybrid frequency domain/continuous wave clinical system for breast imaging," *Med Phys,* vol. 30, *(2),* pp. 235-247, 2003. . DOI: 10.1118/1.1534109.

[19] B. W. Pogue *et al*, "Instrumentation and design of a frequency-domain diffuse optical tomography imager for breast cancer detection," *Opt. Express, OE,* vol. 1, *(13),* pp. 391-403, 1997. Available: https://www.osapublishing.org/oe/abstract.cfm?uri=oe-1-13-391. DOI: 10.1364/OE.1.000391.

[20] A. Farina *et al*, "Time-Domain Functional Diffuse Optical Tomography System Based on Fiber-Free Silicon Photomultipliers," *Applied Sciences,* vol. 7, *(12),* pp. 1235, 2017. Available: http://www.mdpi.com/2076-3417/7/12/1235. DOI: 10.3390/app7121235.

[21] Maheswari, Sathiyamoorthy and Amala, "FORWARD MODEL ANALYSIS IN DIFFUSE OPTICAL TOMOGRAPHY USING
RTE AND FEM," *International Journal of Power Control and Computation(IJPCSC),* vol. 8, *(1),* pp. 20-29, Available: https://pdfs.semanticscholar.org/6d1b/65d602c15aaa82aca36f2ec8fea5d49f5398.pdf.

[22] R. Baikejiang, W. Zhang and C. Li, "Diffuse optical tomography for breast cancer imaging guided by computed tomography: A feasibility study," *Journal of X-Ray Science and Technology,* vol. 25, *(3),* pp. 341-355, 2017. Available: https://content.iospress.com/articles/journal-of-x-ray-science-and-technology/xst16183. DOI: 10.3233/XST-16183.

[23] H. Dehghani *et al*, "Near infrared optical tomography using NIRFAST: Algorithm for numerical model and image reconstruction," *Commun Numer Methods Eng,* vol. 25, *(6),* pp. 711-732, 2008. . DOI: 10.1002/cnm.1162.

[24] H. Jiang *et al*, "Optical image reconstruction using frequency-domain data: simulations and experiments," *J. Opt. Soc. Am. A, JOSAA,* vol. 13, *(2),* pp. 253-266, 1996. Available: https://www.osapublishing.org/josaa/abstract.cfm?uri=josaa-13-2-253. DOI: 10.1364/JOSAA.13.000253.

[25] A. Franchois and C. Pichot, "Microwave imaging-complex permittivity reconstruction with a Levenberg-Marquardt method," *Tap,* vol. 45, *(2),* pp. 203-215, 1997. Available: https://ieeexplore.ieee.org/document/560338. DOI: 10.1109/8.560338.

[26] H. Jiang *et al*, "Simultaneous reconstruction of optical absorption and scattering maps in turbid media from near-infrared frequency-domain data," *Opt. Lett. , OL,* vol. 20, *(20),* pp. 2128-2130, 1995. Available: https://www.osapublishing.org/ol/abstract.cfm?uri=ol-20-20-2128. DOI: 10.1364/OL.20.002128.

[27] P. K. Yalavarthy *et al*, "Weight-matrix structured regularization provides optimal generalized least-squares estimate in diffuse optical tomography," *Medical Physics,* vol. 34, *(6),* pp. 2085-2098, 2007. Available: http://dx.doi.org/10.1118/1.2733803. DOI: 10.1118/1.2733803.

[28] S. van de Ven *et al*, "Diffuse Optical Tomography of the Breast: Initial Validation in Benign Cysts," *Mol Imaging Biol,* vol. 11, *(2),* pp. 64-70, 2009. Available: https://www.ncbi.nlm.nih.gov/pubmed/19030937. DOI: 10.1007/s11307-008-0176-x.

[29] B. J. Tromberg *et al*, "Imaging in breast cancer: diffuse optics in breast cancer: detecting tumors in pre-menopausal women and monitoring neoadjuvant chemotherapy," *Breast Cancer Research : BCR,* vol. 7, *(6),* pp. 279-285, 2005. Available: https://www.ncbi.nlm.nih.gov/pubmed/16457705. DOI: 10.1186/bcr1358.

[30] C. Li, *Breast Cancer Detection with Diffuse Optical Tomography.* 2006.

[31] H. Zhang *et al*, "Comparison of Diffuse Optical Tomography, Ultrasound Elastography and Mammography in the Diagnosis of Breast Tumors," *Ultrasound in Medicine and Biology*, vol. 40, *(1)*, pp. 1-10, 2014. Available: https://www.umbjournal.org/article/S0301-5629(13)01016-8/fulltext. DOI: 10.1016/j.ultrasmedbio.2013.09.008.

[32] L. Grazioli *et al*, "Comparison of ultrasound, CT and MRI in the assessment of parotid masses," *European Radiology*, vol. 4, *(6)*, pp. 549-556, 1994. Available: https://link.springer.com/article/10.1007/BF00226828. DOI: 10.1007/BF00226828.

[33] S. R. Arridge and J. C. Hebden, "Optical imaging in medicine: II. Modelling and reconstruction," *Phys Med Biol*, vol. 42, *(5)*, pp. 841-853, 1997.

[34] R. L. Wahl *et al*, "Metabolic monitoring of breast cancer chemohormonotherapy using positron emission tomography: initial evaluation," *J. Clin. Oncol.*, vol. 11, *(11)*, pp. 2101-2111, 1993. . DOI: 10.1200/JCO.1993.11.11.2101.

[35] F. P. Mghanga *et al*, "Fluorine-18 fluorodeoxyglucose positron emission tomography-computed tomography in monitoring the response of breast cancer to neoadjuvant chemotherapy: a meta-analysis," *Clin. Breast Cancer*, vol. 13, *(4)*, pp. 271-279, 2013. . DOI: 10.1016/j.clbc.2013.02.003.

[36] S. R. Cherry, "MULTIMODALITY IN VIVO IMAGING SYSTEMS: Twice the Power or Double the Trouble?" *Annual Review of Biomedical Engineering*, vol. 8, *(1)*, pp. 35-62, 2006. Available: https://doi.org/10.1146/annurev.bioeng.8.061505.095728. DOI: 10.1146/annurev.bioeng.8.061505.095728.

[37] L. Radan *et al*, "The role of FDG-PET/CT in suspected recurrence of breast cancer," *Cancer*, vol. 107, *(11)*, pp. 2545-2551, 2006. . DOI: 10.1002/cncr.22292.

[38] L. Pace *et al*, "Comparison of whole-body PET/CT and PET/MRI in breast cancer patients: lesion detection and quantitation of 18F-deoxyglucose uptake in lesions and in normal organ tissues," *Eur J Radiol*, vol. 83, *(2)*, pp. 289-296, 2014. . DOI: 10.1016/j.ejrad.2013.11.002.

[39] J. Shi *et al*, "Optical molecular imaging-guided radiation therapy part 2: Integrated x-ray and fluorescence molecular tomography," *Med Phys*, vol. 44, *(9)*, pp. 4795-4803, 2017. . DOI: 10.1002/mp.12414.

[40] SPIEDigitalLibrary.org/conference-proceedings-of-spie, "SPIEDigitalLibrary.org/conference-proceedings-of-spie," *Optical Tomography and Spectroscopy of Tissue XII*, vol. 10059, pp. 1005912, 2017. Available: https://www.spiedigitallibrary.org/conference-proceedings-of-

spie/10059/1005912/Gaussian-kernel-based-anatomically-aided-diffuse-optical-tomography-reconstruction/10.1117/12.2252786.short. DOI: 10.1117/12.2252786.

[41] Vasilis Ntziachristos *et al*, "MRI-Guided Diffuse Optical Spectroscopy of Malignant and Benign Breast Lesions1," vol. 4, pp. 347-354, 2002. Available: https://www.ncbi.nlm.nih.gov/pmc/articles/PMC1661680/. DOI: 10.1038/sj.neo.7900244.

[42] G. Wang and J. Qi, "PET image reconstruction using kernel method," *IEEE Trans Med Imaging*, vol. 34, *(1)*, pp. 61-71, 2015. . DOI: 10.1109/TMI.2014.2343916.

[43] Pepper and Heinrich, *The Finite Element Methods, Basic Concepts and Applications.* (2nd ed.) .

[44] K. Ho-Le, "Finite element mesh generation methods: a review and classification," *Computer-Aided Design*, vol. 20, *(1)*, pp. 27-38, 1988. Available: http://www.sciencedirect.com/science/article/pii/0010448588901388. DOI: 10.1016/0010-4485(88)90138-8.

[45] S. Fantini *et al*, "Assessment of the size, position, and optical properties of breast tumors in vivo by noninvasive optical methods," *Appl. Opt. , AO*, vol. 37, *(10)*, pp. 1982-1989, 1998. Available: https://www.osapublishing.org/ao/abstract.cfm?uri=ao-37-10-1982. DOI: 10.1364/AO.37.001982.

[46] M. Jermyn, H. Ghadyani, M.A. Mastanduno, W. Turner, S.C. Davis, H. Dehghani, and B.W. Pogue, "Fast segmentation and high-quality three-dimensional volume mesh creation from medical images for diffuse optical tomography," *J. Biomed. Opt*, 2013.

[47] M. Schweiger and S. Arridge, "The Toast++ software suite for forward and inverse modeling in optical tomography," *J Biomed Opt*, vol. 19, *(4)*, pp. 040801, 2014. . DOI: 10.1117/1.JBO.19.4.040801.

[48] H. Si, "TetGen, a Delaunay-Based Quality Tetrahedral Mesh Generator," *ACM Trans. Math. Softw.*, vol. 41, *(2)*, pp. 11:1–11:36, 2015. Available: http://doi.acm.org/10.1145/2629697. DOI: 10.1145/2629697.

[49] G. S. Loening AM, "AMIDE: A completely free system for medical imaging data analysis," *Journal of Nuclear Medicine*, 2001.

[50] U. Alqasemi, H. S. Salehi and Q. Zhu, "Method for estimating closed-form solutions of the light diffusion equation for turbid media of any boundary shape," *Journal of the Optical Society of America. A, Optics, Image Science, and Vision*, vol. 33, *(2)*, pp. 205, 2016. Available: http://www.ncbi.nlm.nih.gov/pubmed/26831771. DOI: 10.1364/JOSAA.33.000205.

[51] N. Iftimia *et al*, "A compact, parallel-detection diffuse optical mammography system," *Review of Scientific Instruments*, vol. 74, *(5)*, pp. 2836-2842, 2003. Available: https://aip.scitation.org/doi/abs/10.1063/1.1568558. DOI: 10.1063/1.1568558.

[52] Z. Lin *et al*, "CCD-camera-based diffuse optical tomography to study ischemic stroke in preclinical rat models," in 2011/02/17, Available: https://www.spiedigitallibrary.org/conference-proceedings-of-spie/7896/78960R/CCD-camera-based-diffuse-optical-tomography-to-study-ischemic-stroke/10.1117/12.875883.short. DOI: 10.1117/12.875883.

[53] S. Fantini *et al*, "Assessment of the size, position, and optical properties of breast tumors in vivo by noninvasive optical methods," *Appl Opt*, vol. 37, *(10)*, pp. 1982-1989, 1998.

[54] Nannan Cao, Arye Nehorai, and Mathews Jacob, "Image reconstruction for diffuse optical tomography using sparsity regularization and expectation-maximization algorithm," *Opt. Express 15*, pp. 13695-13708, 2007.

[55] H. Dehghani *et al*, "Three-dimensional optical tomography: resolution in small-object imaging," *Appl. Opt. , AO*, vol. 42, *(16)*, pp. 3117-3128, 2003. Available: https://www.osapublishing.org/ao/abstract.cfm?uri=ao-42-16-3117. DOI: 10.1364/AO.42.003117.

[56] P. K. Yalavarthy *et al*, "Structural information within regularization matrices improves near infrared diffuse optical tomography," *Optics Express*, vol. 15, *(13)*, pp. 8043, 2007. Available: http://www.ncbi.nlm.nih.gov/pubmed/19547132. DOI: 10.1364/OE.15.008043.

[57] A. H. Golnabi *et al*, "Comparison of no-prior and soft-prior regularization in biomedical microwave imaging," *J Med Phys*, vol. 36, *(3)*, pp. 159-170, 2011. Available: https://www.ncbi.nlm.nih.gov/pmc/articles/PMC3159222/. DOI: 10.4103/0971-6203.83482.

[58] R. Landauer, "Johnson-Nyquist noise derived from quantum mechanical transmission," *Physica D: Nonlinear Phenomena*, vol. 38, *(1)*, pp. 226-229, 1989. Available: http://www.sciencedirect.com/science/article/pii/0167278989901978. DOI: 10.1016/0167-2789(89)90197-8.

[59] H. Vavadi and Q. Zhu, "Automated data selection method to improve robustness of diffuse optical tomography for breast cancer imaging," *Biomedical Optics Express*, vol. 7, *(10)*, pp. 4007, 2016. Available: https://www.ncbi.nlm.nih.gov/pubmed/27867711. DOI: 10.1364/BOE.7.004007.

[60] D. Zhu *et al*, "Comparison of Regularization Methods in Fluorescence Molecular Tomography," *Photonics*, vol. 1, *(2)*, pp. 95-109, 2014. Available: https://search.proquest.com/docview/1540825477. DOI: 10.3390/photonics1020095.